UNIL | Université de Lausanne
Faculté des géosciences
et de l'environnement

Master of Science in Geography

Changes in sediment connectivity following glacial debuttressing in an Alpine valley system

Mancini Davide

Under the direction of Prof. Stuart Lane
Expert: MER. Christophe Lambiel

Maîtrise universitaire ès sciences en géographie | Janvier - 2019

Acknowledgements

Several people have been of great help to me over the course of this project and over my years at the UNIL.

Firstly, I would like to especially thank Prof. Stuart Lane for giving me the chance to work with him and his team, for his explanations, suggestions and motivation during this project. His guidance helped me in all my master thesis' steps; from the field campaign to the correction of my English. This work would not have been possible without him.

My second big thank goes to PhD candidate Gilles Antoniazza for his huge help with collecting and processing lidar data and for the precious advice given to me along the realization of my thesis.

Furthermore, I really want to thank all my classmates from Ticino for having made awesome and unforgettable my university's years in Lausanne. You are the best!

Last, but not least, I am sincerely grateful to my family for all the sacrifices made for me and my education. I dedicate this work to you all.

Thank you!

Index

Abstract

It is now largely recognized that current climate warming strongly impacts glacierized catchments globally. Increasing atmospheric temperature, in addition to other climatic parameters, influence both the cryosphere and the hydrosphere in high mountain regions, and so drives glacier recession. The latter is the most palpable and visible environmental transformation produced by climate change in mountain regions. The resulting deglaciated landscape is essentially composed of debris accumulations (e.g. frontal/lateral morainic ridges) and steep valley sidewalls usually till-covered (e.g. debris-mantled slopes). These landforms can be in an unstable state because glacier thinning causes glacial debuttressing, and subsequent failure of material. This may be exacerbated by interaction with rainfall or snowmelt events. The period during which geomorphic processes rework glacigenic deposits, modifying landscape in response to non-glacial conditions, is called the "paraglacial period". In our study, we used two distinct temporal scales to investigate the geomorphological evolution of the Glacier d'Otemma Little Ice Age moraine to rapid glacier recession at the paraglacial time scale. In an historical perspective between 1964 and 2009, and largely based upon archival aerial digital photogrammetry methods, we studied how the geomorphic response to non-glacial conditions, induced by glacial debuttressing, impacted hillslope sediment connectivity. We found that gradual moraine denudation, notably caused by gullying and headward erosion during the glacier thinning phase, promoted better sediment connectivity on the valley side slopes but reduced connectivity at the hillslope-alluvial plain scale due to the formation of large alluvial fans. In this context, we also highlighted two important considerations: first, the presence of a morainic bastion as the primary sediment cascade's debris source strongly influences gully morphology evolution; and second, connectivity improvement through gully headward erosion is not linear but conditioned by the exposure of bedrock topographic buffers. Over a shorter time-scale, we conducted lidar surveys during the glacier ablation season in order to quantify shorter time scale geomorphic change within the LIA lateral moraine section and at the hillslope-alluvial plain scale. We did not find significant changes in this regard, but this fact pointed to the significance of high magnitude events for sediment reworking processes and consequently landscape evolution.

Keywords: Climate warming; Glacial debuttressing; High mountain regions dynamics; Paraglacial; Sediment connectivity; Historical evolution.

Resumé

Il est aujourd'hui reconnu que le réchauffement climatique a un impact important sur les bassins versants englacés du monde entier. L'augmentation de la température atmosphérique, en outre à d'autres paramètres climatiques, possède un impact sur la cryosphère et l'hydrosphère dans les régions de haute montagne, entraînant ainsi la récession des glaciers. Cette dernière est la transformation environnementale la plus visible du changement climatique dans les régions de montagne. Le paysage déglacé est essentiellement composé d'accumulations de débris (par exemple les crêtes morainiques) et de parois de vallée recouvertes de till (*debris mantled slopes*). Ces formes de relief peuvent être instables, car l'amincissement des glaciers provoque la destitution des glaciers et la conséquente perte de cohésion des matériaux. Cela peut être exacerbé par une interaction avec les précipitations ou la fonte des neiges. La période dans laquelle les processus retravaillent les dépôts glacigéniques, modifiant le paysage en réponse à des conditions non glaciaires, est appelée "période paraglaciaire". Dans notre étude, nous avons utilisé deux échelles temporelles pour étudier l'évolution géomorphologique de la moraine latérale du Petite Age Glaciaire du Glacier d'Otemma suite à la récession rapide du glacier. Dans une perspective historique entre 1964 et 2009, largement basée sur la photogrammétrie historique d'archive, nous avons étudié comment la réponse géomorphologique à des conditions non-glaciaires impacte la connectivité sédimentaire du versant. Nous avons constaté

que la dénudation progressive de la moraine, causée par le ravinement et l'érosion régressive lors de l'amincissement du glacier, favorisait une meilleure connectivité sédimentaire sur la moraine mais une dégradation à l'interface entre le versant et la plaine alluviale en raison de la formation de grands cones alluviaux. Dans ce contexte, nous avons également souligné deux considérations importantes: premièrement, la présence d'un bastion morainique en tant que source principale de débris de la cascade sédimentaire influence fortement l'évolution de la morphologie des ravines; et deuxièmement, l'amélioration de la connectivité par l'érosion fluviale n'est pas linéaire mais conditionnée par l'exposition de tampons topographiques du substrat rocheux. Sur une période plus courte, nous avons effectué des scans lidar en manière de quantifier les transformations géomorphologiques qui adviennent soit sur moraine du PAG, soit entre la moraine et la plaine alluviale pendant la saison d'ablation du glacier. Nous n'avons pas trouvé informations significatives à cet égard, mais ce fait a mis en évidence l'importance des événements de grande magnitude pour la remobilisation des sédiments et l'évolution du paysage.

Mots-clés: Rechauffement climatique; *Glacial debuttressing*; Dynamique des hautes regions de montagne; Paraglacial; Connectivité sédimentaire; Evolution historique.

1. Introduction

High mountain regions are strongly sensitive to climate change. The rapid recession of Alpine glaciers and permafrost zones following current atmospheric temperature rise is well documented (Haeberli et al., 1997; Haeberli and Beniston, 1998; Fischer et al. 2014, 2015). Since the end of the Little Ice Age (LIA), mean annual atmospheric temperatures (MAATs) increased by about +2°C, generating negative mass balance trends and consequently ice volume loss (Bauder et al., 2007; OcCC, 2007; Fischer et al., 2015). European alpine glaciers lost 50% of their surface between 1850 and 2000 while Swiss glaciers, based on the last Swiss glacier inventory of 2010, experienced smaller retreat of about 42% (Paul et al., 2004; Zemp et al., 2006; Fischer et al., 2014).

Glacial retreat leaves a landscape characterized by oversteepened slopes and unconsolidated sediment accumulations often in an unstable state, and acting as potential sediment sources (Ballantyne, 2002a,b). This transition from glacial to non-glacial conditions is called "paraglacial", referring to the geomorphic processes activated by the removal of glacial support (glacial debuttressing) until a new and more stable deglaciated state develops (Church and Ryder, 1972; Porter et al., 2010). During this phase, an increase in the availability of glacigenic deposits and geomorphic process efficiency result in rapid acceleration of the sediment cascade, which in turn lead to a change in catchment spatial configuration and the onset of processes with very different sediment flux rates (Ballantyne, 2002a; Cossart and Fort, 2008; Mercier et al., 2009). In general, the geomorphological consequences of glacier retreat are well known in the scientific literature: on oversteepened rockslopes, strength release caused by decreasing glacier pressure may result in large rockfalls (Cossart et al., 2008; McColl, 2012; McColl and Davis, 2013), while on morainic accumulations, sediment reworking is primarily driven by water, in particular by debris flows, forming complex gully systems (Ballantyne and Benn, 1994; Lane et al., 2017). This may be followed by alluvial and debris fan development, evolving towards a more stable geomorphic state at the end of the paraglacial period (Church and Ryder, 1972; Mercier, 1997, 2008; Ballantyne, 2002a,b).

However, less consideration has been given to understanding the way in which sidewall to valley bottom connectivity evolves during the paraglacial phase following a rapid glacier recession (Beawert and Morche, 2014; Heckmann et al., 2016). Recent studies suggest that glacier retreat could increase catchment's longitudinal and latitudinal connectivity in two main ways. First, as proglacial stream networks have important and continuous sediment transport rates compared to supraglacial and subglacial streams, glacier recession and subsequent proglacial stream development may increase down valley transport of hillslope-sourced sediments compared to a situation where sediments are deposited on the glacier surface (Lane et al., 1996, 2017; Orwin and Smart, 2004; Uhlmann et al., 2013). Second, glaciation may lead to the presence of landforms which interrupt the sediment cascade, such as lateral moraine ridges, and these act as intermediate sinks (Brardinoni and Hassan, 2006; Cossart and Fort, 2008; Fryirs, 2013; Lane et al., 2017). Such interruptions are unlikely to be permanent, as glacier retreat and thinning leads to base level fall that can activate gullying, eroding in a headward direction (Schiefer and Gilbert, 2007; Cossart and Fort, 2008) and eventually breaking through these buffers (e.g. Lane et al., 2017). In recently deglaciated environments without vegetation cover, gullying may be an important agent for sediment downslope transport because glacially derived material is poorly sorted including a relatively easily eroded fine sediment fraction (Borselli et al. 2008; Trevisani et al., 2012). This fluvial process is therefore a critical control upon sediment flux during the paraglacial period (Lane et al., 2017).

Given the above, this *mémoire* is focused on the evolution of one of the Glacier d'Otemma's Little Ice Age lateral moraine (Wallis, Switzerland) in a context of rapid climate warming and glacier recession. The work is subdivided into two main timescales. The first one, based on the decadal timescale, considers the historical geomorphological evolution of the lateral moraine since 1960 during the phase of glacial debuttressing. The aim is to determine the impacts that gully headward

erosion, generated by the progressive ice body retreat, has on valley sidewall sediment cascade and connectivity. It uses archival digital aerial photogrammetry methods to follow the temporal evolution of both sediment sources and sinks, quantifying how the sediment cascade has evolved over time. The second one, limited to a single summer month, seeks to quantify current sediment flux, especially between the LIA lateral moraine and the alluvial plain, using repeat Terrestrial Laser Scanning (TLS) surveys.

2. Methodology

2.1 Study site

The proglacial margin of the Glacier d'Otemma is located in Val de Bagnes (Wallis) in the South-West Swiss Alps at an altitude of 2450 m a.s.l., just below the lower limit of the discontinuous permafrost belt (Lambiel and Reynard, 2001; Deluigi et al., 2017) (figure 1). It is characterized by a braided proglacial river and unvegetated LIA lateral moraines, about 200 m above the valley floor. The moraine is a consequence of glacier advance in periods within the Little Ice Age (between 1350 and 1850) and progressively exposed to the atmospheric conditions with the ongoing glacial recession. The study is focused on a 300 m length of the right lateral moraine exposed South-South East. Directly above the study area there is a morainic bastion, built up by the Glacier de la Grande Lire. This landform clearly represents the main source of sediment supplying the sediment cascade of the study area. The moraine is itself partly discontinuous as there are some zones where morainic accumulation did not occur and there are bedrock exposures. Directly above the LIA limit, gravitational and torrential processes accumulated some debris reworking sediments from the bastion (figure 1).

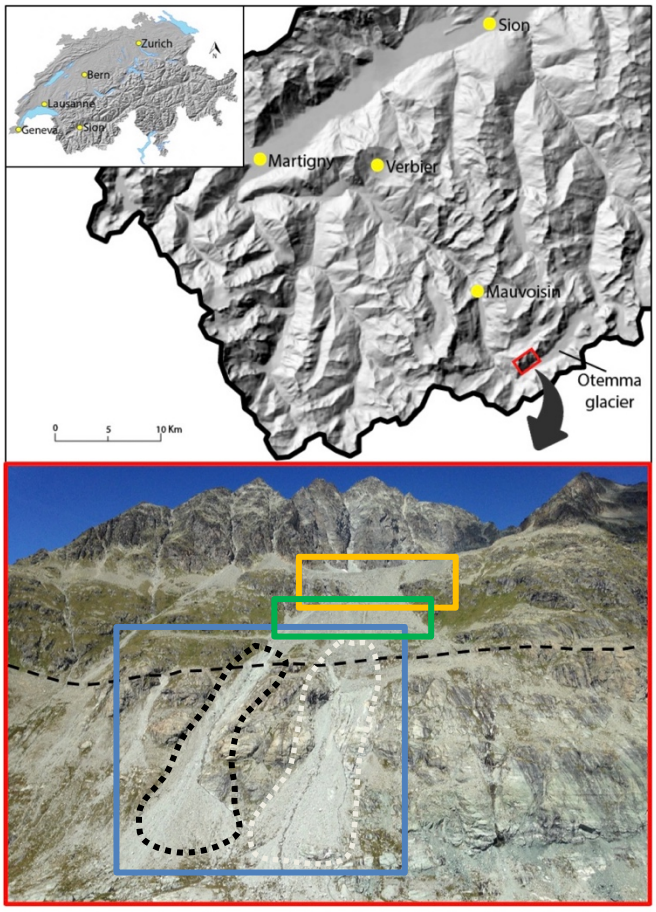

Figure 1: Location of the study area (red square) and image of the valley sidewall in 2017. Blue square highlight the LIA sector where our study is focused, the dotted black line refers to SS1, while the gray one to SS2. Dashed line represents the LIA limit, the orange square refers to the Glacier de la Grande Lire morainic bastion and the green square to the debris accumulation above the LIA limit. Sources of the images: Swiss and Wallis DEMs are provided by SwissTopo; image of the lateral moraine by Davide Mancini.

The *mémoire* has a particular focus on two geomorphological sub-systems. The first (SS1), located in the more downslope part of the study area between two massive rock outcrops, is characterized by a well-developed torrential transport system connecting the morainic bastion to the alluvial cone (black dotted line in figure 1). The second (SS2) is situated on the central part of the study area just below the morainic bastion and it consists of a complex geomorphological system with a sediment cascade composed of an important sediment accumulation at the head of the gully system (gray dotted line in figure 1).

The focus is valuable as the Glacier d'Otemma has a negative mass balance continually since the end of the LIA (figure 2) and, unlike other systems in the region, did not see temporary re-advance in the 1970s and 1980s (Bauder et al., 2007, Fischer et al., 2015). Thus, it provides an analogue for the continual glacier recession we are currently witnessing in Alpine environments. Quantitatively, since the end of the LIA, the Glacier d'Otemma lost about 60% of its volume and 40% of its surface (Lambiel et Tolon, in press). Since the 1880s, the glacier has retreated by -2210 m, forming two main stages. The first, between 1880 and the end of 1960s, is characterized by a cumulative recession of about -530 m, corresponding to a mean rate of -6.2 m/year. The second, over recent decades comprise between 1970 to present, shows a glacier snout retreat of about -1680 m and a mean rate of -36.5 m/year (GLAMOS, 2016). This very rapid recession translates into an increase in the rate of debuttressing, such that slower and more gradual adjustment to ice thinning and eventual retreat is replaced by much more sudden ice loss. There are no studies until this one that have looked at how moraines respond to such rapid recession.

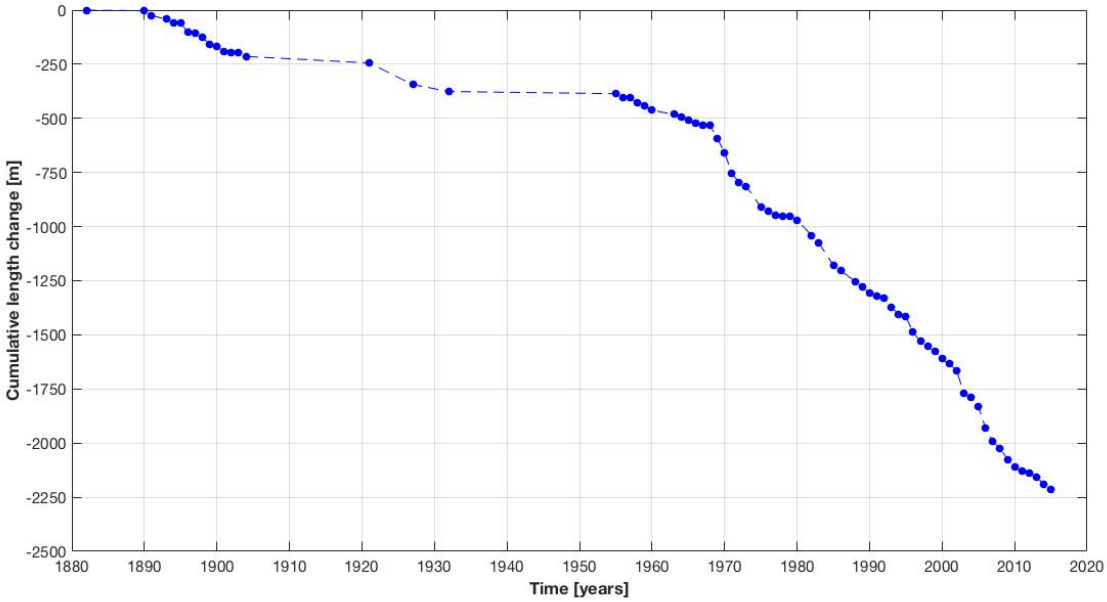

Figure 2: Gacier d'Otemma cumulative retrait since 1880. Data source: GLAMOS (2016).

2.2 Methodology and methods

2.2.1 Overview

The lateral moraine's geomorphologic changes are studied both quantitatively and qualitatively using two different remote sensing techniques: one focused on an historical time-scale and one on a contemporary temporal scale (figure 3). This choice was made to identify the development of different geomorphological processes and forms, which have different time-scales.

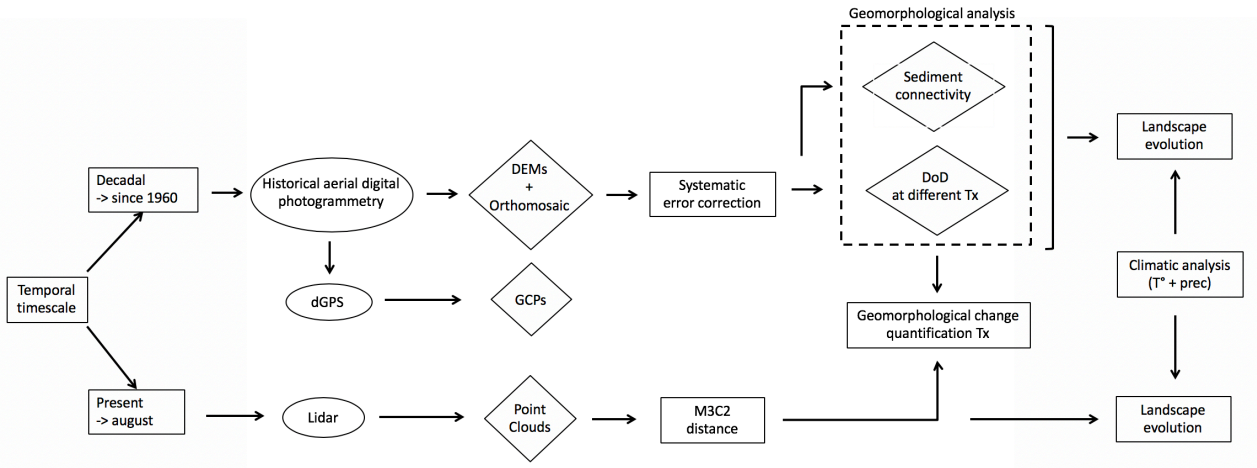

Figure 3: schematic view of the methodology.

As aerial imagery was available from the 1960s, the historical timescale investigated is decadal. To determine the geomorphic evolution of the LIA moraine, archival digital photogrammetry technique was applied to historical aerial images to produce Digital Elevation Models (DEMs) for seven distinct years (T_X). The associated DEMs can be affected by random and systematic errors, related to survey quality, surface composition, topographic complexity and interpolation methods affecting elevation values (Lane et al., 1994; Lane, 1998; Hancock, 2006; Heritage et al., 2009), and this requires error management which is explained below. Once the DEMs were corrected, they were used for two different purposes. First, DEMs of Difference (DoDs) were used to quantify the patterns of erosion and deposition for different epochs. Second, assuming the hydrological control as a main factor for sediment reworking, we conducted a hydrological sediment connectivity analysis (after Lane et al., 2017). We were interested in hydrologically driven sediment connectivity in a transient landscape, with a specific focus on the modes by which former glacial and new paraglacial geomorphological forms impact its evolution. These analyses were combined with detailed geomorphological information, conducted through geomorphological mapping and analysis of elevation profiles, with the aim of determining the evolution of interuptions to the sediment cascade through time.

For the contemporary (i.e. within-season) timescale, we acquired two lidar scans during a field campaign that took place from August 9th to 20th 2017. Surface changes were detected directly from acquired point clouds by adopting the Multiscale Model to Model Cloud Comparison (M3C2) plugin of CloudCompare (Lague et al., 2013).

2.2.2 Climatic context

Geomorphic changes in high mountain regions are strongly dependent on climatic conditions. Climatic data were provided by the Swiss Office of Meteorology and Climatology (MeteoSwiss), but longer-term records are available for only few locations usually located below an altitude of 1000 m a.s.l. The Otemma's measurement station is the closest one to the study area but, due to the short duration of operation (since 2011) and recording of precipitation only, it is utilizable only to analyze the morphological changes at the seasonal timescale. For the decadal timescale, it is necessary to use records collected from more distant measure stations, under the conditions that they are positioned in similar geographic context in order to avoid altitude and topographic effects.

For both atmospheric temperature and precipitation, we chose to use records derived from the Grand St. Bernard (GSB) measure station located 20 km from the Glacier d'Otemma's proglacial area. Our choice is justified by two motivations. First, the GSB station is the closest one with both long-term (since 1864 for temperature and since 1901 for precipitation) and homogenized data. This means that

records have been constantly calibrated to account, for example, for changes in instrumentation or station position, which could influence their quality. Note that other climatic measure stations are located near Otemma but, due to their non-homogenized data, short-term length or limited parameters measured, they cannot be use in our study (table 1; figure 4).

Table 1: location and characteristics of the nearest climatic station from Otemma. Source: MeteoSuisse.

Station	Distance from study area (km)	Altitude (m a.s.l)	Type of data	Data available since
Bourg St. Pierre	15	1822	Prec.	1900
Evolène	21	1825	Prec.; Temp.	1986
Fionnay	13	1500	Prec.	1997
Grand St. Bernard	19	2472	Prec.; Temp. (homogenized)	1901 for prec. 1850 for temp.
Martigny	31	461	Prec.	1960
Montagnier	22	839	Prec. (homogenized)	1907
Orsières	23	929	Prec.	1901
Otemma	1.5	2357	Prec.	2011
Sion	33	482	Prec.; Temp. (homogenized)	1864
Zermatt	28	1638	Prec.; Temp.	1892 for prec. 1959 for temp.

Prec. = precipitations; Temp. = atmospheric temperature

Second, the study area and the GSB station are located at similar altitudes (2466 m a.s.l. for the Otemma's foreland and 2468 m a.s.l. for GSB), both close to the southern Alpine divide (figure 4). This geographical context is very important because there are strong precipitation gradients with distance from this divide, related to the predominant directions of travel of rain bearing weather (Baeriswyl and Rebetez, 1997).

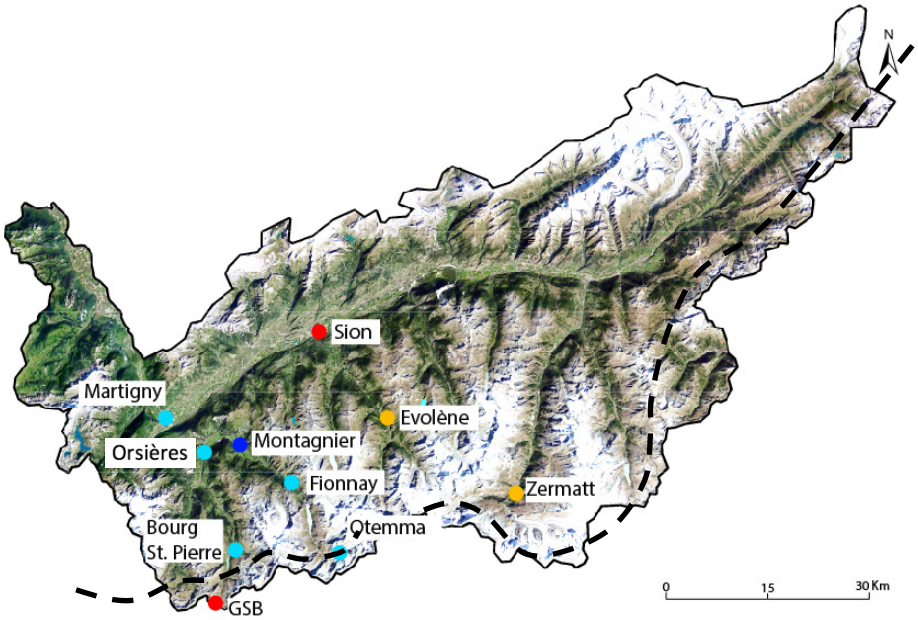

Figure 4: spatial view and topographic context of the Otemma's nearest climatic stations. Dashed black line represents the southern Alpine divide; red points show long term stations recording homogenized atmospheric temperatures and precipitation data; orange points highlight station recording non-homogenized atmospheric temperature and precipitation; blue point represent station with long term homogenized precipitation data; light blue points indicate stations limited to non-homogenized precipitation data. Source of background image: SuisseTopo (modified).

2.2.3 Archival digital aerial photogrammetry

Photogrammetry is a long-established remote sensing technique that has now been proven for the reconstruction of long-term geomorphic changes in Alpine environments, including river-floodplain systems (e.g. Lane et al., 2010; Bakker and Lane, 2017), glacial (e.g. Gabbud et al., 2016; Lane et al., 2017; Mölg and Bolch, 2017) and periglacial areas (e.g. Kääb and Vollmer, 2000; Schiefer and Gilbert, 2007; Micheletti et al., 2015a). The principles of applying photogrammetry to historical archival imagery are outlined in Lane et al. (1993). Bakker and Lane (2017) report their application using Structure-from-Motion (SfM) photogrammetric method and it is their approach that is followed here.

The historical images used in this work were provided by the Swiss Federal Office of Topography (Swisstopo) which since 1927 constantly records the entire country. Images for seven distinct dates between 1964 and 2009 were purchased with the corresponding camera calibration certificate. Due to the length of time, and the associated development of photograph technologies, images were obtained with a wide range of cameras with different technical characteristics (table 2).

Table 2: main characteristics of used aerial image datasets and internal camera orientation parameters.

Date	Camera type	# images	Overlap [%]	Scale [1 : x]	Scan resolution [µm]	Ground pixel resolution [m]	Calibrated focal length [mm]
1964	Lens 29 11.5 AG	14	60	1:17700	21	0.37	115.29
1970	Lens 174 15 AG	9	60	1:8600	21	0.18	132.10
1977	Lens 3004 15 UAG II	17	60	1:8600	14	0.12	153.02
1983	Lens 13018 15/4 UAG	17	60	1:8600	14	0.12	153.37
1988	Lens 13018 15/4 UAG	18	60	1:8600	14	0.12	153.37
1995	Lens 13220 15/4 UAG-S	13	80	1:8600	14	0.12	152.52
2009	Lens 13220 15/4 UAG-S	14	60	1:19800	14	0.19	152.52

Camera flying heights during image acquisition varied between 4100 m and 6000 m generating different image scales, between 1:8600 and 1:19800, degrees of overlap and ground pixel resolutions. The data provided were scanned to photogrammetric standard by Swisstopo with a resolution of 21 µm (1964) or 14 µm (remaining imagery). For all datasets, images were taken with a large format photogrammetric camera (18x18 cm for 1964 and 23x23 cm all other imagery) in black and white at the end of summer (between the end of August and the beginning of September), when snow cover is normally minimal at the altitude of the area of interest in this study.

Archival digital photogrammetry was applied using the SfM photogrammetry following Bakker and Lane (2017). With archival imagery, SfM photogrammetry (figure 5) estimates parameters in the collinearity equations that relate the imagery geometry to the ground surface geometry using a very large numer of common tie points, extracted and conjugated using machine vision methods (Lowe, 1999; Westoby et al., 2012; Fonstad et al., 2013; Micheletti et al., 2015b,c). This reduces substantially the constraints on image orientation and location associated with traditional method in terms of both resolving the bundle adjustment and then subsequent image matching to extract conjugate point pairs whose coordinates are estimated. Althought camera calibration certificates were available for all cases here, it also allows self-calibration of the internal camera geometry, so allowing use of archival imagery of unknown geometry (Aguilar et al., 2013). However, Bakker and Lane (2017) questioned the reliability associated with this process and showed that was important to use the established camera calibration certificates to define internal camera geometry. The first step in the SfM technique is the automatic tie-points determination using a SIFT algorithm able to identify conjugate features in multiple images even if they have very different pixel resolutions and color gradients (Lowe, 1999; Fonstad et al., 2003). With a large number of individuated conjugate points, the collinearity equations are resolved in an arbitrary coordinate system which included an iterative self-calibration, here restricted to the external camera parameters of every image, that is their relative orientation (Fonstad et al., 2013; James and Robson, 2014). Finally, the last steps are the densification of a point cloud

using the multi-view stereo matching algorithm (MVS) and its transformation from an arbitrary coordinate system into a real coordinate system by adding several Ground Control Points (GCPs) (Fonstad et al., 2003; Smith et al., 2016).

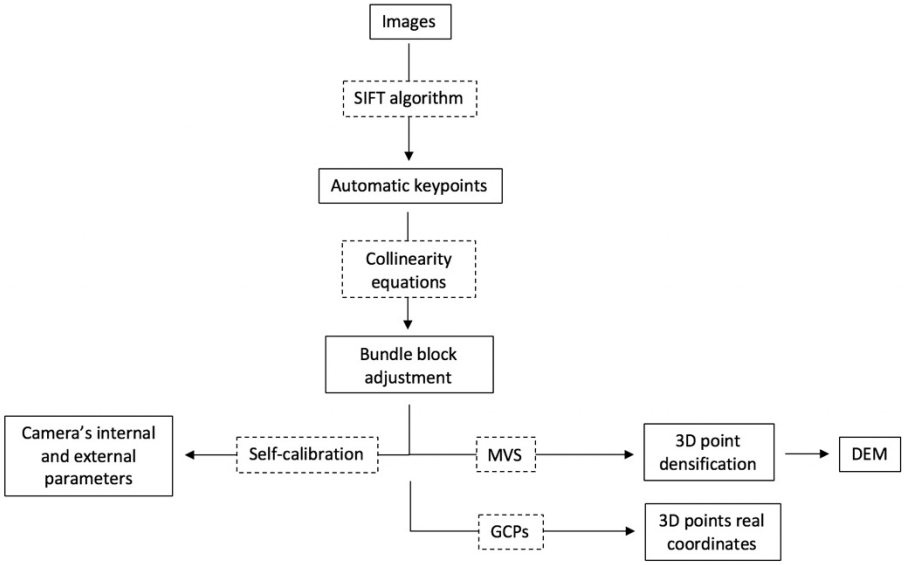

Figure 5: schematic workflow for SfM photogrammetry. Based on Fonstad et al. (2013).

Even if the SfM approach seems easier and more precise than conventional photogrammetry thanks to the self-calibration mode, this method can generate systematic errors in resulting DEMs. Indeed, aerial images are commonly close to nadir and have overlaps designed to optimize application of traditional digital photogrammetry. It is well established that this image geometry is weak for determination of external camera parameters (Lane et al., 2004; Wackrow and Chandler, 2008; James and Robson, 2014; Bakker and Lane, 2017), and this means that for effective archival image application using SfM it is necessary to refer to more traditional approaches, including the use of GCPs earlier in the process, when camera parameters are estimated (Bakker and Lane, 2017). That said, research suggests that if undertaken correctly, SfM archival photogrammetry can provide comparable results to those of more classical digital photogrammetry (Gomez et al., 2015; Bakker and Lane, 2017; Mölg and Bolch, 2017).

2.2.3.1 Application of SfM photogrammetry in this study

To compute photogrammetric 3D models of past landscapes, we used the software Pix4D©. This is a commercial SfM software platform most commonly used for processing images obtained by drone surveys (www.pix4d.com). Pix4D has been already used to perform archival aerial photogrammetry in geomorphological studies focused on landscape evolution through time in periglacial (e.g. Lane et al., 2017), fluvial (e.g. Bakker and Lane, 2017), glacial (e.g. Mölg and Bolch, 2017) and soil erosion (e.g. Castillo et al., 2014) projects.

Following the procedure of Bakker and Lane (2017), we use the camera calibration certificate to specify the calibrated focal length (table 2) and the calibrated parameters for tangential and radial lens distortion. We used the Swiss CH1903 coordinate system and we manually inserted the initial coordinates (X,Y) of the principal point position of every uploaded image. To aid the initial solution of the collinearity equations, we included 3 GCPs (Fonstad et al., 2013). The GCP collection followed Micheletti et al. (2015b). A Trimble© R10 dGPS was used establishing the base station on a fixed point and left record for 12 hours. These coordinates were than corrected *post hoc* using the continuously recording dGPS network SwissPos©, meaning that the data were accurately tied into the

CH1903. In the field, dGPS measurements of clearly identifiable boulders and bedrock outcrops were measured in a real-time kinematic survey, with data point precision of ±0.01m in the horizontal and ±0.02m in the vertical. These were also corrected *post hoc* to the SwissPos-corrected based station. The choice of GCPs locations had the initial goals of: (i) a good distribution across the study area (Küng et al., 2011, Javernick et al., 2014) and (ii) long-term stability (Micheletti et al., 2015b). The latter had to be met and this meant in practice we had to relax the former, but noting that with the SfM photogrammetric method, the bundle adjustment uses conjugate features identified from across the area of interest, so increasing the robustness of estimations in zones beyond where the GCPs were measured. In total, we were able to measure 13 stable GCPs. Due to the stability criterion, they are concentrated in the southern part of the LIA proglacial margin (figure 6).

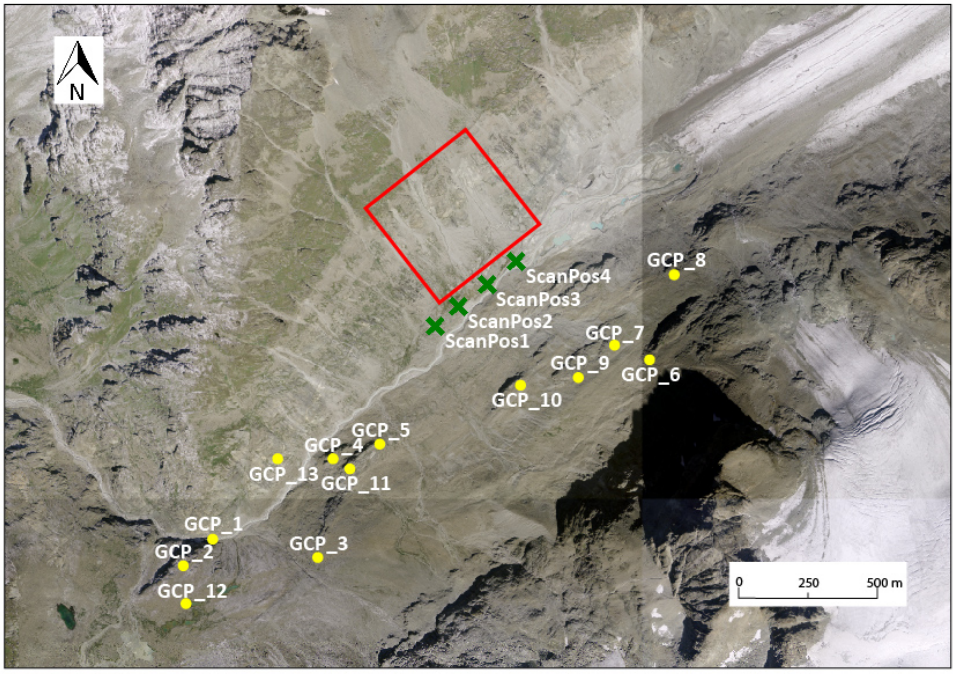

Figure 6: spatial distribution of both GCPs (yellow points) and lidar scan positions (green crosses); red square refers to the location of the study area. Source of background image: SwissTopo.

Once an initial solution has been obtained using 3 GCPs, additional GCPs were manually added iteratively to improve the solution and to minimize the RMSE in the solution. Then a point cloud, with the associated DEM, was generated.

2.2.3.2 DEM post-processing

Once point clouds had been generated, we investigated the presence of random and systematic errors, especially tilt or dooming effect (James and Robson, 2012, 2014). These latter may be generated by the incorrect solution of the collinearity equations (Lane et al., 2000; James and Robson, 2012; Micheletti et al., 2015b) but it has also been shown that even with an accurate solution, random error in estimated parameters can lead to systematic DEM error, which becomes notable when consecutive DEMs are compared (Lane et al., 2004).

To identify and then manage error, we undertook two analyses: (i) analysis of the residual errors in the GCP coordinates as compared with their measured ones; and (ii) identification of stable zones (notably bedrock outcrops) which in theory should show no elevation change of significance in the timescale of our study. The latter is needed as it has been shown that a large number of GCPs distributed across the study area are required to characterize error fully (Lane et al., 2004).

Systematic errors were removed by co-registration onto a single reference point cloud using CloudCompare© (Miller et al. 2008; Micheletti et al., 2015c; Bakker and Lane, 2017). Visually, the best point cloud appeared to be that of 1983 and all point clouds, limited to the area of interest, were co-registered onto this one. We identified features that had to be stable during the study period (primarily bedrock outcrops but also large boulders) and used it in the iterative adjustment method in CloudCompare to minimize the RMSE between each point cloud and that for 1983. To further reduce linear systematic DEMs error, we also adopted a multi-regression method using stable zone elevation values in order to better fit individual DEMs to the reference.

After systematic error correction, 1 m resolution DEM grids were created in Arcmap 10 using kriging. This interpolator is recognized to be the best solution for complex landscape surface data because of its ability to conserve larger-scale topographic detail (Moore et al., 1991; Holmes et al., 2000). Finally, resulted DEMs were clipped to the study area and used to detect both historical surface geomorphological changes, using the Université de Lausanne geomorphological legend (Lambiel et al., 2016), and evolution of the hydrological sediment connectivity.

2.2.3.3 Calculation of DEMs of difference

DEMs of difference (DoD) were calculated to determine erosion and deposition patterns (Lane et al., 2003). This latter is based on a simple matrix subtraction (T_{X2}-T_{X1}) between DEMs (Brasington et al., 2003; Lane et al., 2003). In practice, we then needed to account for residual uncertainties in the dataset (Brasington et al., 2003), related to (i) the quality of individual points in point clouds, (ii) the density of points available to represent the surface, (iii) the distribution of points within the study area and (iv) the interpolation method used to generate regular surface within points (Lane et al., 1994; Lane, 1998; Hancock, 2006; Heritage et al., 2009). In our case, we generated very high point densities, with very few zones of interest not covered, and so the primary focus was upon the uncertainty due to the quality of individual points. Thus, we used a simple error propagation method (after Brasington et al., 2003 and Lane et al., 2003) to investigate the propagation of error in individual DEMs in DEMs of difference, which was defined as the level of detection needed for an elevation change to be juged as significant. After Lane et al. (2003) this was defined as:

$$\mathrm{LoD} = t\sqrt{(\sigma_{DEM1})^2 + (\sigma_{DEM2})^2} \quad (1)$$

where: LoD = Limit of Detection threshold
t = Student's confidence interval threshold value (1.96 at 95% or 1 at 68%)
σ_{DEM1} = standard deviation of DEM_1 Z error
σ_{DEM2} = standard deviation of DEM_2 Z error

The standard deviation of individual DEMs error was calculated from a sample of 98 Z values measured from spatially distributed stable zones recognizable on all georeferenced DEMs. We took a confidence interval for t of 68% as it is established that a high confidence interval tends to overlook smaller magnitude but spatially homogeneous changes (Wheaton et al., 2010) and because this threshold produced visually sensible patterns of erosion and deposition.

2.2.7 Hydrological sediment connectivity analysis

Sediment connectivity is defined as the degree to which sediments can flux through the landscape, and in particular between sediment sources and downstream areas (Cavalli et al., 2013). However, as we worked on hydrological sediment connectivity, is it better to define it as the water mediated transfer of sediment between two different compartments of the catchment 'sediment cascade (Fryirs, 2013). Where sediment flux becomes disconnected, a sediment sink is formed and serves to remove sediment from the cascade for variying lengths of time (Fryirs, 2013; Bracken et al., 2015). In our study, sediment connectivity analysis has two main related objectives. The first is to detect the evolution of both lateral moraine sediment sources and sinks, as well the water-related sediment transport paths, starting from the analysis of DoDs and orthoimages. The focus is on how landscape evolution following glacial debuttressing impacted hydrological connectivity within the LIA lateral moraine and at the hillslope-proglacial alluvial plain scale. The second one, similar to Lane et al. (2017), seeks to investigate the distinction between natural and artificial sediment disconnections and its evolution through time. Sediment disconnection may be confused with DEM-related noise, especially where surface roughness is lower (Borselli et al., 2008; Cavalli et al., 2013; Lane et al., 2017). In our study, we define natural disconnection as the flow path obstruction by a geomorphological feature that leads to a reverse slope (e.g. due to glacial or paraglacial landforms), while artificial disconnection is that caused by DEM noises. In geomorphological researches, the identification of sediment flow paths starting from DEM data is commonly undertaken by forcing flow accumulation function throught filling all depressions regardless of their nature, and which risks removing disconnection that is natural rather than artificial (Arnold, 2010). As we are interested in determining the impact of the evolution of the moraine morphology on sediment connectivity between 1964 and 2009, we applied the methodological approach proposed by Lane et al. (2017) to our photogrammetry acquired DEMs, which captures how the level of hydrological connectivity evolves as a DEM is progressively filled. If there is a transition from low to high upslope contributing areas close to the theoretically expected DEM noise, it is likely that a flow path is hydrologically connected. Where the transition occurs at greater levels of fill, so it becomes more likely that the connection is a true connection, the greater the level of fill, the greater the probability.

The Lane et al. (2017) approach looks at how hydrological connectivity evolves with progressively different levels of DEM fill. The TopoToolbox (Schwanghart and Kuhn, 2010), is used to apply Holmgren (1994) flow routing to calculate the upslope contributing areas (*A*: defined as the area upslope of a surface element that drains to that element; Rieger, 1998) with different levels of DEM fill. The Holmgren routing uses:

$$FD_{(j)} = \frac{(tanB_j)^x}{\sum_{j=1}^{8}(tanB_j)^x} \quad (2)$$

where: FD(j) = proportion of hydrological flow in direction j
B = slope gradient between the central cell and the cell in direction j
x = variable exponent varying between 0 and infinity

Equation 2 determines for each DEM cells the proportion of flow going in a specific direction. For x=0 flow is equally distributed in all directions regardless of slope; for x=1 flow is proportionally divided to all downhill cells in function of slope gradient (multi-directional flow) and for $x = \infty$ all runoff is directed along the line of steepest descent (i.e. D8 algorithm) (Quinn et al., 1991; Holmgren, 1994; Lane et al., 2017). In our study, we decided to use variable x values (x=1,2,4,8,16 and 32) to asses their effects. The fill value begins at 0.1 m and is then increased dyadically to a maximum of 102.4 m. In case of artificial disconnection (dotted line in figure 7), we would expect a rapid increase in *A* when the level of fill reachs values comparable to DEM noise (σ_{2009}) because the critical fill

threshold (*K*) to get through noises is reached. However, in the presence of natural disconnection (dash-dotted line in figure 7), the *A* increase may be later (*K*>DEM precision) and also achieved in a number of steps if there a number of natural disconnections of different magnitude.

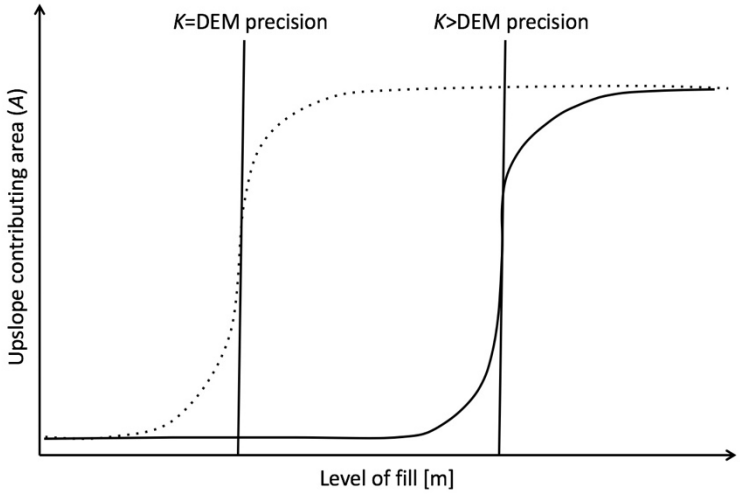

Figure 7: hydrological sediment connectivity model for artificial (dotted line) and natural (dash-dotted line) disconnectivity in function of upslope contributing area (A), fill level and DEM precision (K) (Lane et al., 2018 – modified).

To apply the method, accumulation is determined for cross-sections on the hillslope. By comparing accumulation for these cross-sections for two different dates is it possible to understand how hydrological connectivity has evolved through time. Following Lane et al. (2018) the geomorphological system may experience two main important changes. If in the most recent date perfect connection (i.e. a rapid increase in *A* close to the levels of noise in the DEM) is reached at lower levels of fill, it implies that there has been erosion of the associated hydrological disconnection, such as through gullying (dotted line figure 8). If the transiction occurs later, or the value of *A* becomes higher, it suggests that connection evolved through both fluvial erosion and the re-organisation of the basin (such as the capture of a basin upstream, increasing *A*, but which is itself impacted upon by some disconnections, shifting the increase in *A* to a higher level of fill) (dash-dotted line figure 8). It is also possible that there has been the development of blockages along a flow path if the level of fill required to achieve perfect connection increases.

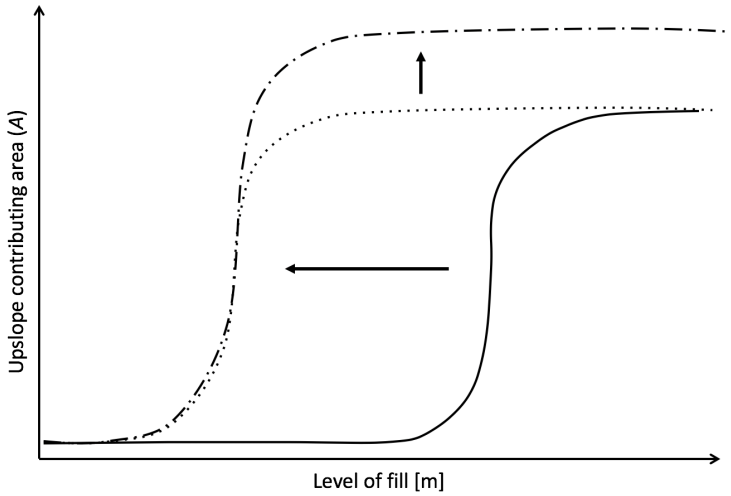

Figure 8: hydrological sediment connectivity evolution; base level fall and headward erosion propagation (dotted line) and upslope basin reorganization (dash-dotted line) (Lane et al., 2018 – modified).

2.2.8 Terrestrial laser scanning surveys

Geomorphological change investigation at the contemporary time-scale was conducted using Terrestrial Laser Scanning (TLS) technique. The steep gradient of the valley sidewalls combined with the complex topography of the study area explain this choice, notably given possibly shading that might occur with aerial imagery (Beawert and Morche, 2014; Goodwin et al., 2017). Lidar as a tool to detect surficial geomorphological changes has already been adopted in several projects, including proglacial margins (e.g. Carrivick et al., 2013), periglacial regions (e.g. Abermann et al., 2010), glacial recession (e.g. Gabbud et al., 2015) and landslides events (e.g. Jones, 2006).

2.2.8.1 Data acquisition

During our field campaign, we used a RIEGL VZ-6000© to conduct two scans (August 13th and 20th) among which occurred small rainfall episodes. To compute distances, the lidar emits a beam of light in the near infrared range (NIR), 1064 nm in our settings, and measures the time required for the signal to return to the source after the reflection from a target object, in this case the moraine. Data output are point clouds where each point has specific coordinates in a determined projected system. The RIEGL VZ-6000 is a powerful instrument able to conduct measurements up to 6000 m from its position with a large frequency interval, from 23'000 meas./s at 30 kHz to 222'000 meas./s at 300 kHz, and a laser beam footprint of 15 mm at the light source (RIEGL Laser Measurements Systems, 2015). Choosing the right parameters is an important task because the reflecting surface and the distance from scan may influence the return signal's quality and intensity. In our case, we worked on a moraine composed of different types of rock (essentially gneiss and schists; Burri et al., 1999) with varying size (boulders, cobble, pebble and sand). The reflectance of this kind of landscape is about 60% in the NIR wavelength thanks to its low water content at the survey distances typical of this study (RIEGL Laser Measurements Systems, 2015). Concerning scan distance, the moraine was easily accessible from different viewpoints and, to cover the overall view of the study area, a distance from the moraine of 250 m was sufficient (figure 6). Nevertheless, due to the large moraine surface (ca. 300 m width and 200 m high), four scan positions were needed, also aiding the reduction of occlusion effects (figure 6). Due to these characteristics, we conclude that a measurement frequency of 150 kHz could produce good results.

2.2.8.2 Point clouds manipulation

Point cloud manipulation was necessary to data for the CloudCompare M3C2 plugin, allowing us to compute distances between different point clouds.

First, we used RiscanPro's multistation adjustment (MSA) to associate point clouds on each day for the four scan positions into a single local coordinate system. We registered clouds acquired from different scan positions coupling point pairs associated with stable zones, such rock outcrops and large boulders. The MSA target was a RMS error within the range ±5 cm and with a normal distribution. At this stage, the point cloud was also cleaned to remove the reflections caused by atmospheric dust. Once the data were oriented into the same coordinate system, they were merged into a single point cloud using CloudCompare. This procedure was performed on both scan days, producing two co-registered point clouds, each with c.300 million data points. To reduce data handling times, the point clouds were segmented at the upper LIA limit to produce c.100 million points per cloud. Finally, the Noise Filter tool was used to detect isolated points in space. This approach is founded on distances from a locally-fitted plane, which represent in the best way the real surface (CloudCompare, 2015).

2.2.8.3 Point clouds distances using M3C2

In addition to allowing for co-registration of datesets, CloudCompare allows computation of distances between clouds sampled at different times. There are three options: Cloud-to-Cloud (C2C), Cloud-to-Mesh (C2M) and Multiscale Model to Model Cloud Comparison (M3C2) (Barnhart and Crosby, 2013). These techniques compute distances directly from point clouds, rather than using prior DEM generation (gridding and interpolation) (Lague et al., 2013).

The C2C method has two options both based on the closest point distance. The first uses the original clouds directly (PC) (figure 9A), while the second one, before the distance computation, applies a local model to a determined radius area (least squares plane, 2D triangulation or height function) of the reference cloud to generate a plane representing in the best way the real topographic surface (figure 9B). As the method is founded on the closest point distance, the resulting C2C distances *L* could be very sensitive to cloud roughness (σ) and densities, especially because these factors influence the local model's algorithm outputs (Girardeau-Montaut et al., 2005; Lague et al., 2013). Surface change using the C2M technique is calculated starting from distances between a point cloud and the vertex of a reference meshed surface (M) generated with the Delaunay triangulation method (figure 9C; Olsen et al., 2010; Barnhart and Crosby, 2013). As shown by Lague et al. (2013), the main defect of this approach is the incapacity to consider the local orientation, represented by the normal vector. Consequently, distance computation may be dependent on point cloud densities and roughness variation such in the case of complex topography (Kazhdan et al., 2006; Schürch et al., 2011).

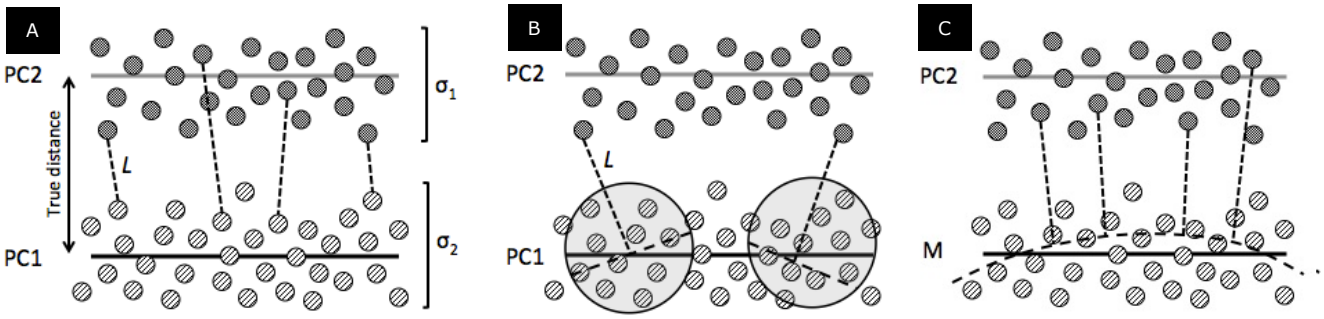

Figure 9: existing distance computation methods between point clouds; A) Cloud-to-Cloud distance, B) closest point distance to local model distance and C) Cloud-to-mesh distance (C2M).

The M3C2 is a plugin developed by Lague et al. (2013) and is currently considered the best tool to minimize systematic error propagation in point cloud distance analyses because it is based on an algorithm that is more local scale than the other cloud distance computation techniques. The M3C2 procedure requires three distinct data preparation steps to calculate distances (figure 10). Step 1 defines several core points *i* on the reference point cloud (PC1), which are sub-sampled patches of the original point cloud, chosen to require a certain spacing between them (Brodu and Lague, 2012). Step 2 determines the normal vector (N) for each point core *i* fitting a best fit plane using all the neighbor's points *N* that are placed within a radius of *D*/2. In addition, distances between the best-fit plane and the *N* points are used to measure the cloud roughness in each *D* area contouring *i*. Finally, step 3 projects each *i*, from the reference cloud to the compared one, through an operation called projection scale. The latter creates a cylinder of radius *d*/2 centered on *i* with a height *h* oriented by the normal vector intersecting the two-point clouds. The intersection center in the compared point cloud (PC2) determines the position of the core point i_c. Thus, the local distance between point clouds *L* is given by the distance between *i* and i_c. In addition, the intersects of each cloud with the cylinder base *d* define two subsets of points by which standard deviations give the local roughness on the two complementary point cores. Resulting values are used to calculate 95% LoD confidence intervals in

order to determine significant surface changes. The M3C2 outputs are two distinct scalar fields illustrating the distances between the point clouds and the significant changes (distance ≥ ±LoD).

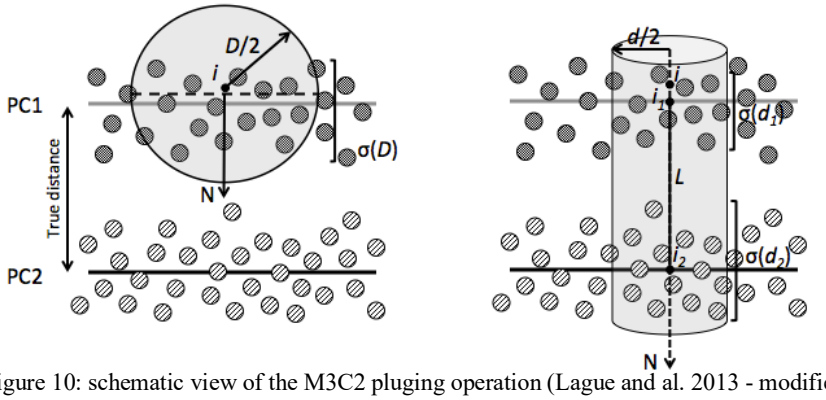

Figure 10: schematic view of the M3C2 pluging operation (Lague and al. 2013 - modified).

Parameter values, in particular *D*, are very important in calculating M3C2 distances because of the algorithm's sensitivity to normal vectors (Lague et al., 2013). In fact, in point clouds representing complex topography, and characterized by variable spatial roughness distribution, a weak *D* value (comparable or smaller than the roughness) could generate an orthogonal vector that overestimate the true distance between the point clouds because of the small number of *i* neighbor points considered in determining the best-fit plane (figure 11).

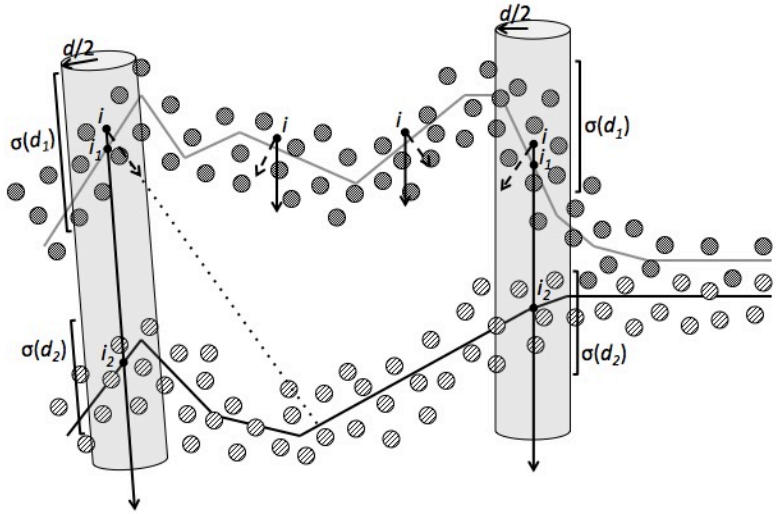

Figure 11: M3C2 in complex topography point clouds (Lague et al., 2013 – modified).

This is exactly the problem that could affect our analysis because our study area is a complex hillslope characterized by unconsolidated glacial debris (cobble to sand size) forming alluvial cone depositions mixed with bedrock exposures. For this reason, following the conclusions of Lague et al. (2013), we chose to work with a *D* value 20-25 times larger than the roughness σ(*D*). The M3C2 parameter values used in our surface change detection analysis are shown in table 3.

Table 3: parameters values used for the M3C2 distance computation.

Parameter	**Value [m]**
i spacing	0.25
Normal scale (*D*)	15
Projection scale (*d*)	1
Projection scale height (*h*)	0.5

3. Results

3.1 Climatic and glacial context

In high glacierized catchments, geomorphological processes are conditioned by both climatic agents and glacial recession, as well as interactions between the two. In order to understand the historical surficial changes more effectively and to quantify sediment connectivity it is important to consider how these main drivers have evolved through time.

Figure 12 shows the Glacier d'Otemma cumulative retreat in relation to the mean atmospheric annual temperature (MAAT) for the GSB since 1900. At the 20th century scale the total GSB MAAT rise of about +1.7°C was not uniformly distributed and there have been four main phases: a relative stable and cold period until the 1940s followed by a rapid warming lasted for about two decades, a cooler epoch between the 1960s and mid-1980s with MAATs between -2.2°C and -0.4°C, and finally again a warmer phase which extends until today characterized by MAATs ranging from -1.6°C and +0.4°C. Since the 1960s, the starting date of our study, the average increase has been of ca. +1.4°C. Since the end of the LIA, the Glacier d'Otemma has been characterized by a negative mass balance, which resulted in a total retreat of about -2110 m with more marked recession rates during the second part of the 20th century. The cumulative length change between 1900 and 1960 shows a reduction of -462 m, corresponding to a mean rate of -6 m/year, while between 1960 to present the increasing in MAATs caused a retreat of -1640 m equivalent to a rate of -32.8 m/year. Since 1880, 79% of the Glacier d'Otemma retreat occurred between 1960 and 2010, and 65% only since 1985 when MAAT started to experience rapid rise. The combination of glacier retreat and thinning is very important because it determines the magnitude of the glacial debuttressing of the lateral moraine and, consequently, the reaction of landscape as geomorphological system.

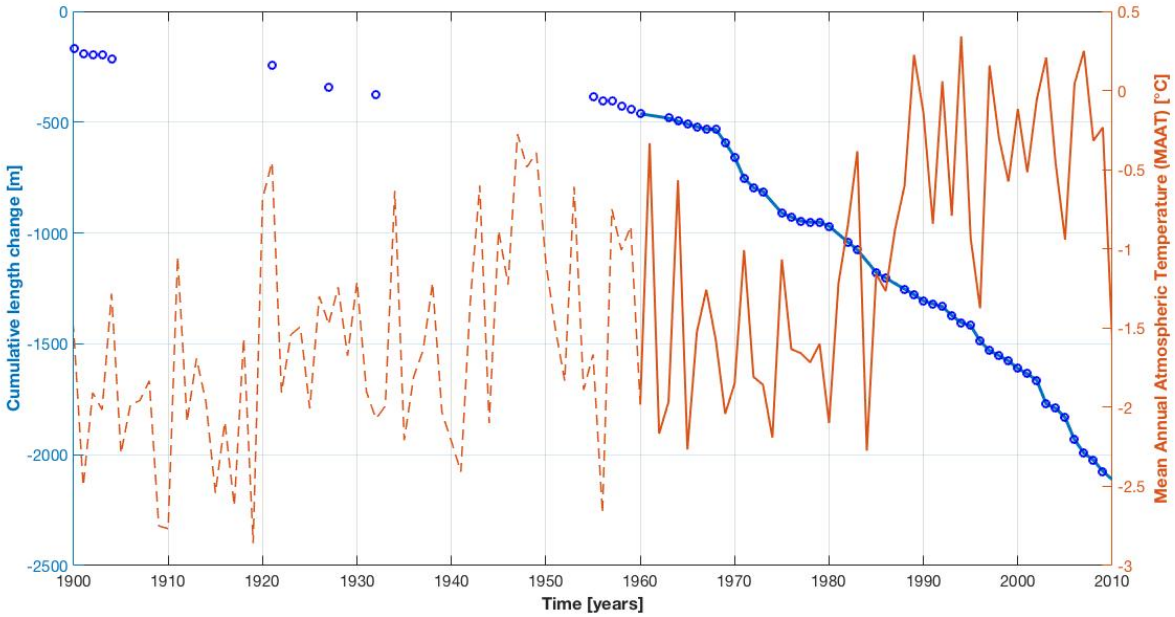

Figure 12: The Glacier d'Otemma's cumulative snout retreat (blue points and solid-dotted blue line) in relation to GSB (dashed and solid orange line) MAAT (dotted and solid-dotted orange line) since 1900.

The continuous phase of glacier recession also results from the progressive shift from solid to liquid precipitation driven by MAAT change, which has reduced snow accumulation during winters. Data published by Micheletti et al. (2015b) based on the GSM-SOCONT model for a location at an altitude of 2700 m a.s.l on the other side of the Pigne d'Arolla, the summit separating Otemma valley from the Arolla valley, show how the accumulated snow at the end of winter, taken here at the end of

March, reflect these patterns (figure 13). The snow depth decrease measured between 1960-1975 and since the mid-1980s follows the MAAT warming that occurred in the 1950s and since the 1980s. Consequently, glacier mass balance has become negative, likely contributing to recession rates (figure 12). The only period characterized by higher snow accumulation coincides with the MAAT cooler period comprised between 1970 and the 1980s.

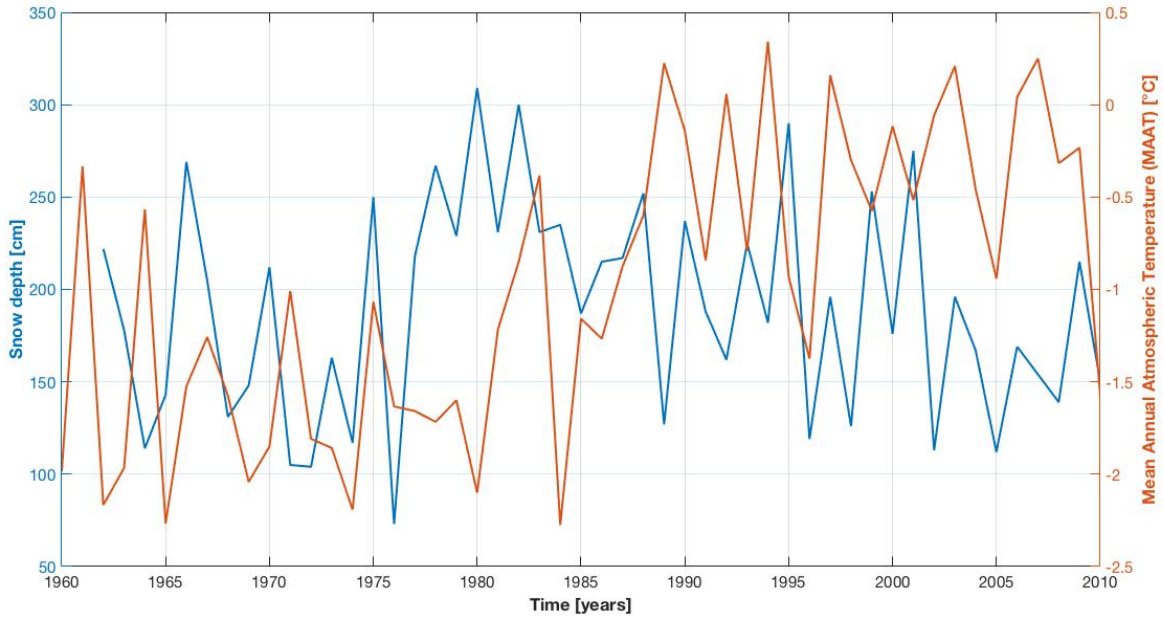

Figure 13: simulated snow accumulation (blue line) at the end of winter for the Arolla region (2700m a.s.l) in relation to MAAT evolution (orange line) since 1960. Data provided by Micheletti et al. (2015b).

At the same time, when combined with MAAT (figure 14), mean annual precipitations experienced three main phases since 1960: a stable state until the mid-1970s followed by an increase lasting until the 2000s, matching with MAAT warming, and finally a weak reduction notably since 2010. The intensification occurred during the 1970s will have important implication for landscape historical evolution.

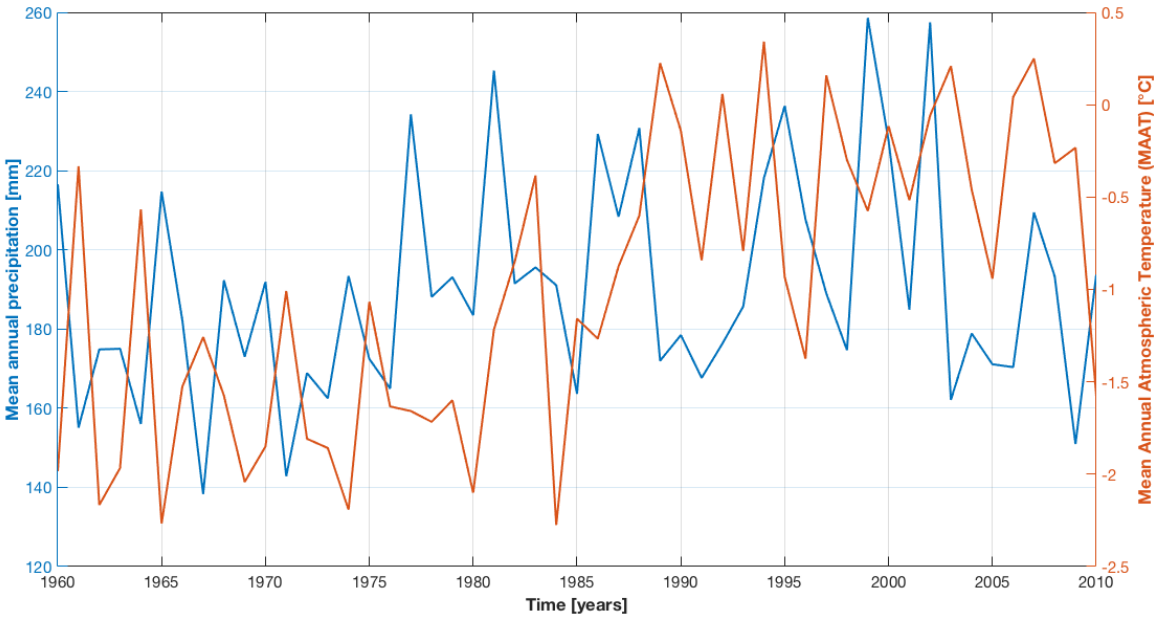

Figure 14: mean annual precipitation (blue line) in relation with MAAT (orange line) recorded at the GSB station since 1960.

3.2 Archival aerial digital photogrammetry

3.2.1 DEM generation

The application of the archival aerial photogrammetry to the historical aerial imagery (table 2), generated seven DEMs. Table 4 summaries the results.

Table 4: Pix4D's parameters and georeferencing error for stable zones marked with GCPs.

Year	# GCPs	Tie-point per image	DEM resolution [m]	Theoretical precision [m]	Mean RMSE [m]	σ error [m]		
						X	Y	Z
1964	4	36341	1.998	±0.37	±0.457	0.193	0.245	0.957
1970	5	81137	0.703	±0.18	±0.062	0.01	0.028	0.159
1977	5	87125	0.608	±0.12	±0.104	0.048	0.190	0.107
1983	8	92290	0.611	±0.12	±0.114	0.085	0.032	0.230
1988	8	91906	0.631	±0.12	±0.369	0.427	0.093	0.605
1995	8	93388	0.641	±0.12	±0.180	0.156	0.151	0.239
2009	4	79913	1.651	±0.27	±0.081	0.031	0.023	0.195

The bundle adjustment used between 4 and 8 GCPs, which is a relatively small number compared to the total surface covered by the aerial images (~29000km^2), and a total number of tie-points per image between 36341 and 93388 points. For 1964, the low number of tie-points is related to the poorer scan resolution (table 2), which reduced image texture and resulted in poorer DEM resolution and higher georeferencing error. DEM resolution is better when a larger number of GCPs and tie-points are available, which is not the case for 1964 and 2009. Table 4 also relates the GCPs mean RMSE to the theoretical precision. In general, the latter is comparable or even higher to the former, but the standard deviation of error of the horizontal (X,Y) and vertical (Z) dimension reveals that there are some additional residual errors. The horizontal errors are generally low, while the vertical one is more relevant as it ranges between 10 and 90 cm. This latter parameter is very important as it controls the levels of detection (LoD) when surfaces are compared. However, with so few GCPs, it is unlikely that these data include systematic errors fully. Inspection of DEMs of difference of stable zones suggested that there were significant changes that should have been zero, and that the DEMs contained residual error (table 5). Tilt correction was applied resulting in a major reduction in systematic error. However, the 1964 DEM due to the poor resolution still shows the highest systematic error.

Table 5: systematic error analysis based on stable zones.

	Error [m]			
	Before correction		After correction	
Year	$\bar{Z}$	σ	$\bar{Z}$	σ
1964	-18.8	±4.0	-0.9	±3.0
1970	-27.5	±4.9	-0.4	±0.5
1977	-9.9	±4.1	+0.4	±0.5
1983	-	-	-	-
1988	+4.9	±3.4	-0.1	±1.5
1995	+21.1	±6.8	-1.0	±1.3
2009	+1.3	±3.6	-0.6	±0.5

Table 6 show the LoD threshold by which DoD were constrained in order to detect only the significant surficial changes occurred between the two dates. The LoD results from equation 1 using the standart deviation of error shown in table 5.

Table 6: Limit of Detection (LoD) for the DEMs of Difference.

Years	68% LoD
1964-1970	±2.99
1970-1977	±1.70
1977-1983	±1.76
1983-1988	±1.74
1988-1995	±2.03
1995-2009	±1.78

3.2.2 Geomorphological evolution (1964-2009)

Figure 15 shows images and geomorphological maps of the lateral moraine in 1964 and 2009.

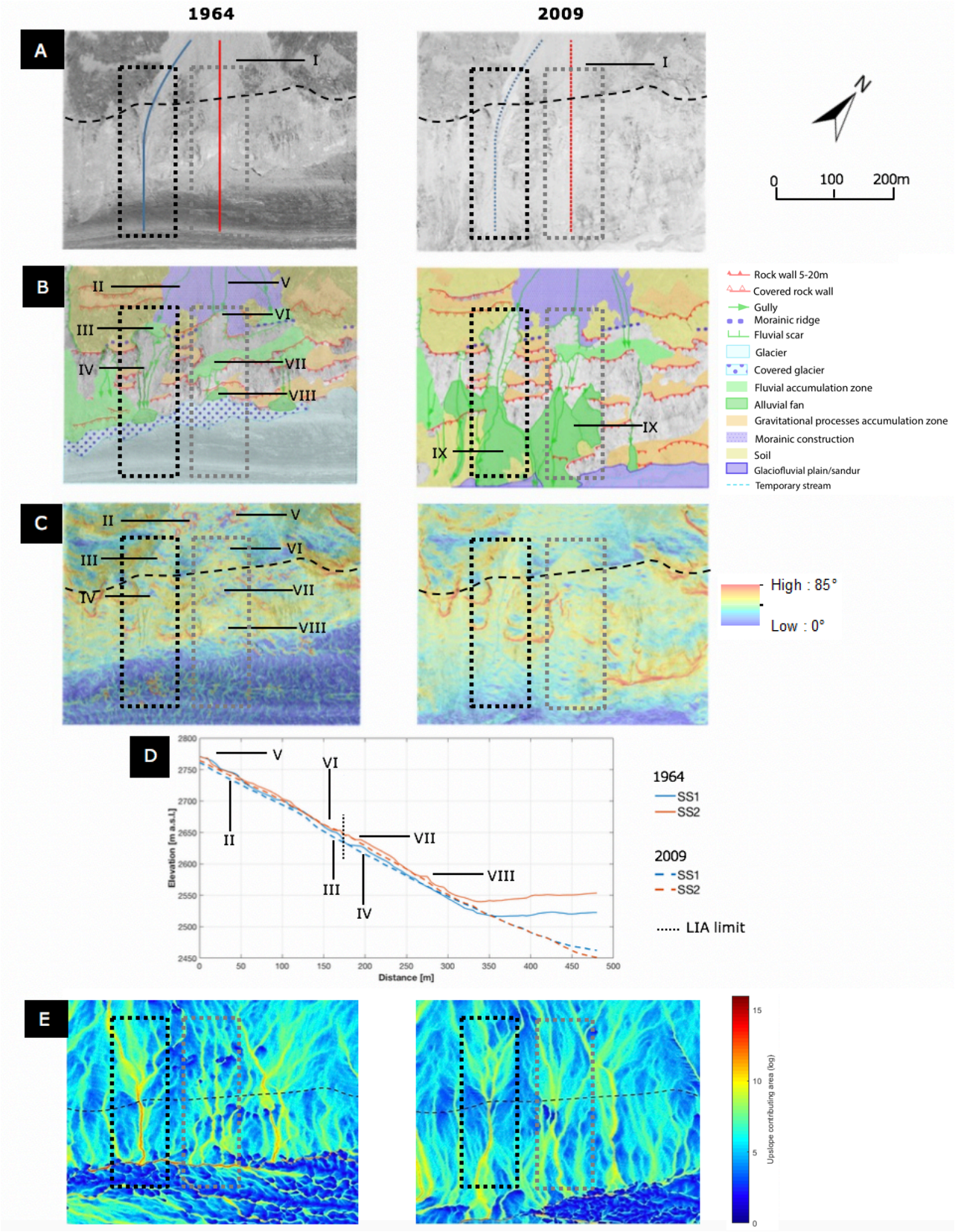

Figure 15: physical and geomorphologic characteristics of the subsystems in 1964 and 2009; A) orthoimage highlighting the location of the two subsystems and of the profile in figure 15D, B) geomorphologic map using the Université de Lausanne legend (Lambiel et al., 2016), C) slope gradient and potential buffers, D) subsystems gradient profiles and E) flow accumulation algorithm calculated with all pits filled with a threshold defined by the σ_{2009} (table 5). Dotted black square refers to SS1, while the gray one to SS2. Dashed line represents the LIA limit.

The LIA limit is shown as a discontinuous morainic ridge (figure 15B). Above it, the hillslope is almost totally covered by a permanent soil vegetation complex, indicating relatively low levels of geomorphic activity. The Glacier de la Grande Lire's morainic bastion is unvegetated and, following a fiel visit, appears to be comprised of non-cohesive sediments (I in figure 15A). It could therefore act as a sediment source to the zones below the LIA limit for both 1964 and 2009. In this latter sector, glacier thinning would represent a major base level fall potentially activating gully headward erosion and subsequent sediment deposition on the valley floor.

The spatial configuration of the hillslope in 1964 is an important aspect to consider because it allows the identification of potential sediment transport paths and buffers. The morainic crest remains, mainly visible on the rock outcrops, are likely to represent barriers for sediment connectivity in both subsystems (figure 15B). Nevertheless, the geomorphological map (figure 15B), elevation profiles (figure 15CD) and flowaccumulation algorithm (figure 15E) show that other potential obstractions to downward sediment transport are anyway present. In SS1, we identified three more buffers (II to IV on figures 15B, 15C and 15D): the flatter zones located on the morainc bastion (II), the flatter area behind the LIA limit (III) and the concave fluvial scar just above the gully system (IV). In contrast, SS2 seems to be affected by a more complex profile resulting in the presence of more potential buffers (V to VIII on figures 15B, 15C and 15D) identified in: the flatter regions on the morainic bastion (V), the fluvial scar with multiple terraces behind the LIA limit (VI), the accumulation at the head of the gullies (VII) and the top of the supraglacial alluvial fan that would have formed on the glacier before its retreat (VIII). In general, all the above-mentionned obstacles are flatter zones constructed by the interaction between the bedrock outcrops and the reworked morainic sediment composing the mantled slope during the LIA and post-LIA epochs. These buffers reduced the mean hillslope's gradient (73% for SS1, 71% for SS2; figure 15D) and strongly impacted the diffusion of its hydrological network (figure 15E).

The situation in 2009 shows the landscape evolution after the glacial retreat and debuttressing. The main important geomorphological change concern the growth of massive alluvial fans at the intersection between the hillslope and the glaciofluvial alluvial plain once filled by the Glacier d'Otemma (IX on figure 15B). These fans may have been aided by greater upslope coupling, following from gully headward erosion activated in response to the glacier thinning, which progressively eroded the debris-mantled slope and accumulations previously identified as potential buffers (figure 15CD).This process also decreased its slope mean gradients (62% for SS1, 65% SS2; figure 15D) and developped a torrential system able to couple even more distant sediment sources (figure 15E). However, subsystems were affected by different intensities of gullying. In SS1 gullies developed upslope reaching the morainic bastion, while in SS2 they eroded without any important upward extention (figure 15B).

Figure 16 quantifies these changes in terms of DEMs of difference for SS1 between 1964 and 2009. During the phase of glacier recession between 1960 and the mid-1970s, is it possible to see substantial glacier loss and thinning, of about -50 m, and hence debuttressing. These resulted in both gullies channel incision and headward erosion (I on figures 16A and 16B). Consequently, reworked sediments accumulated on the underneath (supra-glacial) alluvial fan increasing its basal area and total volume (II on figures 16A and 16B). The erosional patterns describing the alluvial fan during the 1970-1977 period are due to the thinning of the morainic material in response to the glacial surface lowering (figure 16B). At the end of the 1970s, the glacier completely disappeared leading to exposure of the valley bottom (III on figure 16C). But, the stabilization of the hydrological base level does not interrupt landscape's geomorphic assessment to glacial debuttressing. In a general way, during the subsequent decades, the hillslope continued to be shaped by gully headward erosion and the development of slope-base alluvial fan, which now controls the hydrological base level of the subsystem. In this context, since the 1980s, an intenser erosion reworking ca. -2 and -7 m of morainic material per decade, allowed the gully head to extent to the morainic bastion and the removal of the

intermediate sediment sink behind the LIA ridge (I on figures 16D, 16E and 16F). At the same time, the alluvial fan experienced continuous aggradation (ca. +2 and +8 m per decade; II on figure 16D, 16E and 16F) only interrupted during the 1983-1988 period, when we recorded erosional rates comprise between ca. -2 and -7 m (IV on figure 16D). This may be due to the melt of the dead ice, or to development of a braided proglacial river, which thougth the fan base erosion allowed further gully headward erosion (II and IV on figure 16D). Pioneer vegetation developped on the glaciofluvial plain but not on the gully-alluvial fan system indicating that sediment reworking from the morainic bastion is still today very active.

Thus, SS1 experienced a "typical" geomorphological evolution characterited by a constant gully headward erosion, removing buffers and supplying sediment towards the alluvial fan.

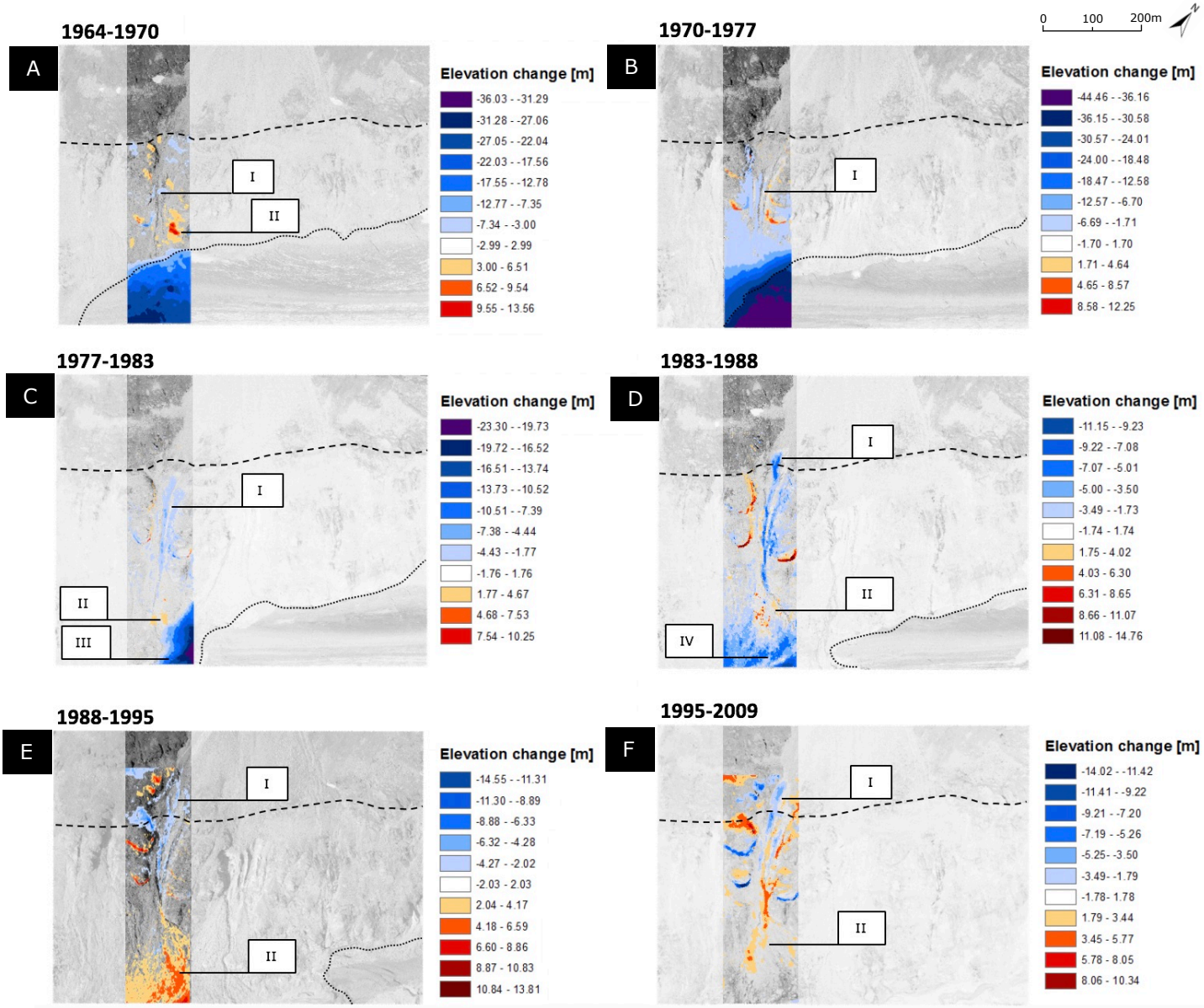

Figure 16: DEM of Difference showing the historical geomorphological evolution of the SS1. Dashed black line refers to the LIA limit and the dotted one to the contact hillslope-glacier at each period. Labels meanings: I = gully headward erosion, II = alluvial fan aggradation, III = valley floor exposure, IV = alluvial fan basal erosion.

Figure 17 shows the historical geomorphological evolution of the SS2. In this case, the fluvial processes occurred in response to the glacial debuttressing are mainly located below the LIA limit, only partially affecting the flatter zone located above the gully system. During the glacier retreat, which lasted until the end of the 1980s, figure 17 suggests a first period characterized by weak fluvial activity (I on figure 17A) followed by increase rates and consequent alluvial fan erosion (I and II in figure 17B and figure 17C). This latter intenser phase is linked to the significant glacier thinning of ca. -60 m, which occurred between the 1970s and the beginning of the 1980s, and is likely to have forced gully erosion and increased down-slope sediment flux. Note that until the exposure of the valley floor, even in this case the alluvial fan shows erosional patterns because its aggradation was smaller than the glacial thinning. From the mid-1980s, similar to SS1, on its down-valley section base level fall to valley floor altitude (III on figure 17D) promoting futher gully headward erosion depositing ca. +2 and +5 m of reworked sediments on the alluvial fan generating a continuous talus within the two subsystems (I and II on figure 17D, figure 17E and figure 17F). But during the 1983-1988 period, up-valley, where the glacier thinning exposed a massive bedrock patch at the interaction with the alluvial plain (IV on figure 17D), fluvially driven erosion appeared to be less intense. Therefore, the alluvial cone began to subdivide into two distinct fans. In the 1988-2009 period further fluvial erosion, encouraged by the complete disappearance of the glacier (III on figure 17E), allowed sediment remobilization. Gully incision (I on figures 17E and 17F) took place with two different spatial intensities: on the upslope section fluvial erosion reworked ca. -6 m of morainic material exposing the underlying bedrock (IV on figure 17E), while on the downslope section, even if recorded rates are more important (ca. -12 m), complete denudation did not take place. The result has been a major alluvial fans aggradation followed, as with SS1, by basal erosion linked to dead ice melting or basal erosion associated to the proglacial stream dynamics (II on figure 17E and V on figure 17F). This event caused further hydrological base level fall reactivating the gully headward erosion (ca. -10 m) in the most downslope area, where the morainic layer is still thick (I on figure 17F). The reworked sediments deposited (ca. +5 m) immediately at the alluvial fan top preventing bedrock exposure (VI on figure 17F). Vegetative colonization took place on the alluvial scar, on the bedrock outcrops and on the alluvial plain without affecting the gully channels and related alluvial fan.

In summary, in SS2 the progressive bedrock exposition on the fluvial system slowed the gully headward erosion maintaining isolation of upslope sediment accumulations.

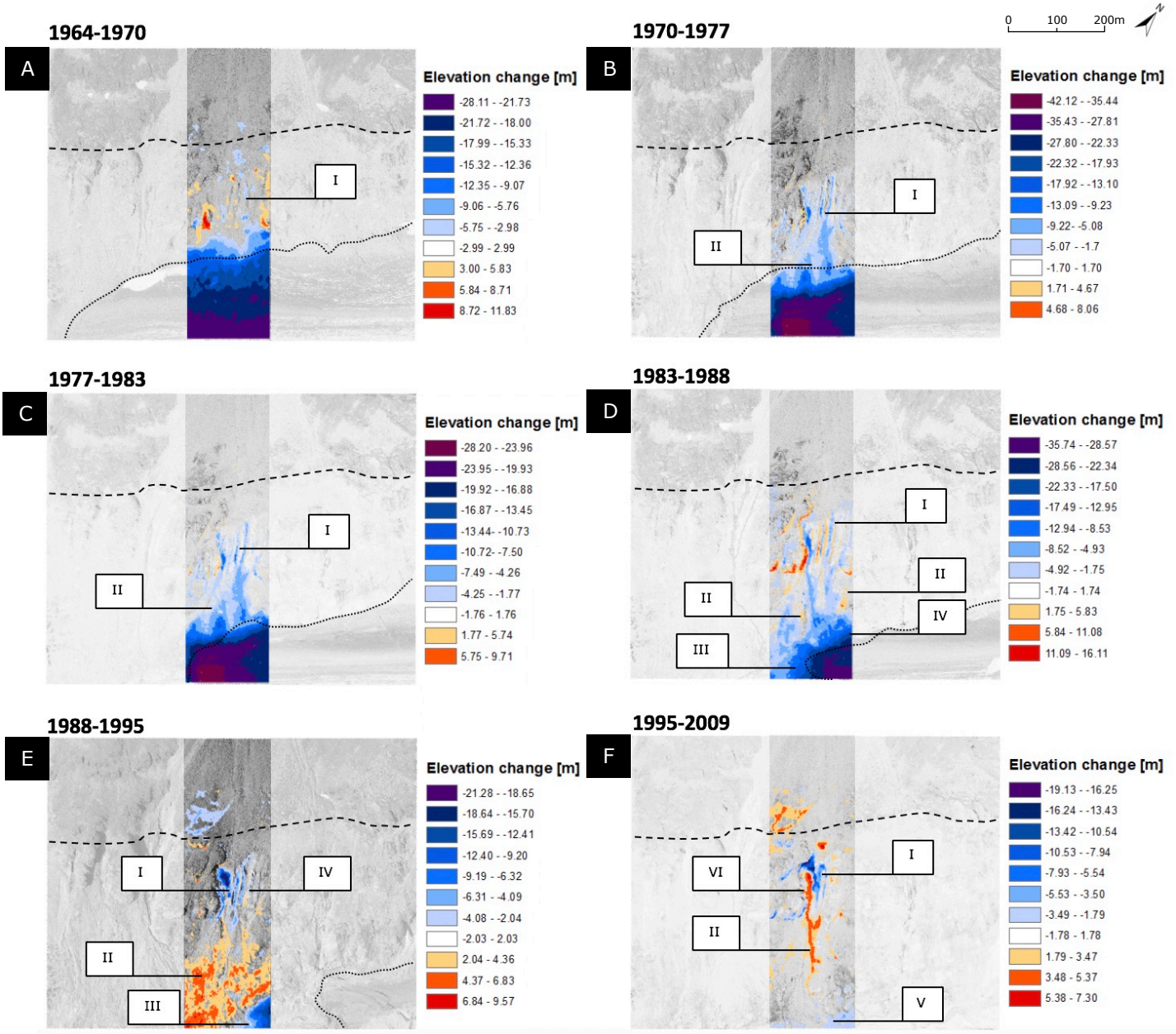

Figure 17: DEM of Difference showing the historical geomorphological evolution of the SS2. Dasched black line refers to the LIA limit and the dotted one to the contact hillslope-glacier at each period. Labels meanings: I = gully headward erosion, II = alluvial fan aggradation, III = valley floor exposure, VI = bedrock patches exposures; V = alluvial fan basal erosion, VI = morainic material aggradation.

3.3 Hydrological sediment connectivity

Given the geomorphic evolution described above, this section seeks to quantify the evolving hydrological connectivity that followed. Figure 18 shows the upslope contributing area for both 1964 and 2009 DEM calculated with all pits filled using a fill threshold defined by the σ_{2009} (table 5).

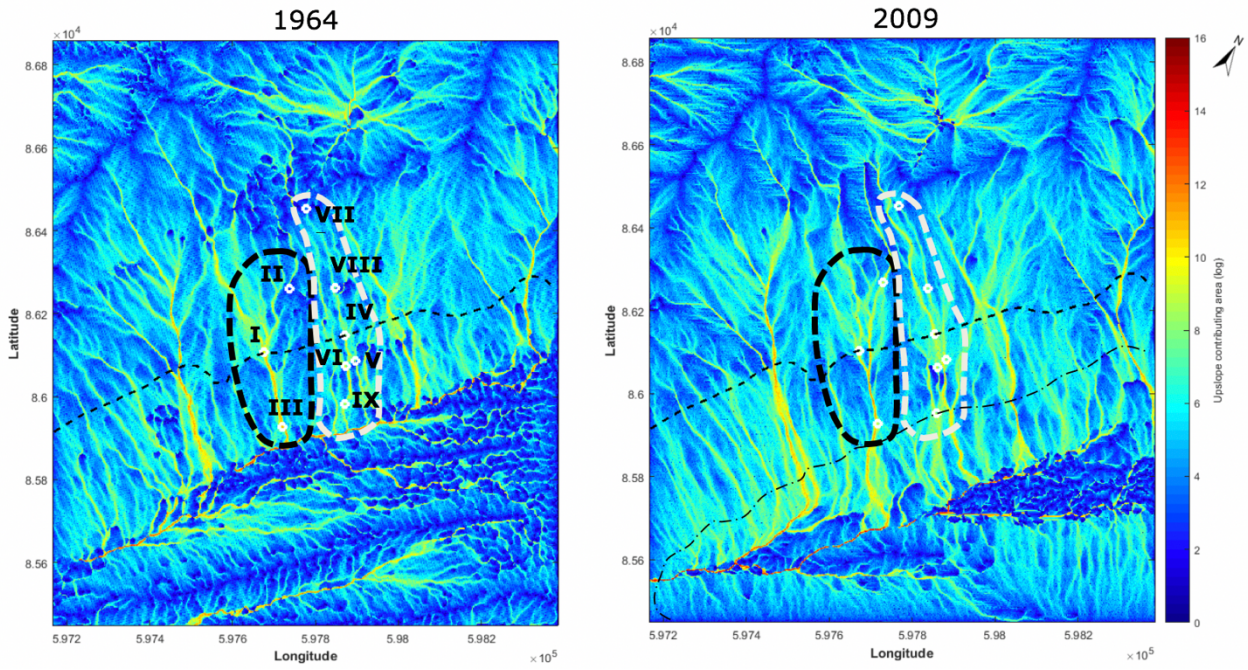

Figure 18: upslope contributing area (Flowacc algorithm) for both 1964 and 2009 DEM with all pits filled. Numbers and circles refer to the potential buffers in figure 15; dotted lines define SS1 (black) and SS2 (gray) limits, dashed black line represents the LIA limit and the dash-dotted black line to the contact glacier-moraine in 1964.

Figure 18 confirms that in 1964 there were drainage patterns present that can also be found in 2009, below the morainic bastion associated with the Glacier de la Grande Lire. The LIA moraine of the Glacier d'Otemma is not-well defined and continuous in 1964, such that there is no clear glacially inherited obstacle to hydrological connection. If there was one, it had been breached before 1960. In 2009, after the complete glacial debuttressing, the efficiency of the hydrological sediment connectivity has generally increased as the hillslope is characterized by higher upslope contributing area values (figure 18 and figure 19). Figure 19, showing the connectivity of difference between 1964 and 2009, highlights that the increase in upslope contributing area appear to be related to the development of the gully network, encouraged by the headward erosion in response to the gradual glacier thinning, connecting previously-separated geomorphological compartments and eroding features once acting as barriers. In fact, the increase in connectivity is most relevant along the gully channels and on the proglacial alluvial plain. In the latter the improvement is probably related to the formation of the proglacial stream system, which have more connection efficiency compared to supraglacial streams, even if in 1964 the contact zone between the hillslope and the glacier represented an important path for the downward hydrological sediment transport. Given this, in 2009 regions having small accumulation values, which coincides with bedrock outcrops, isolated areas of the morainic bastion and disconnections especially in the lower LIA section of SS2 seem to be still significant (figure 18). As a result of the better connectivity, it is possible that increased flux of down-wasted sediments developed the alluvial fans at the hillslope base. Indeed, below the 1964 ice contact line, there is a tendency for flow to become more diffuse (figure 18) suggesting a reduction in connectivity from this fan development.

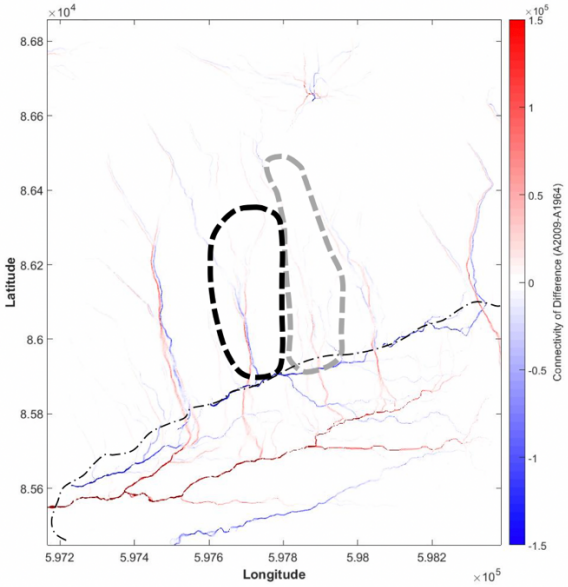

Figure 19: Connectivity of difference between 1964 and 2009. Dotted lines define SS1 (black) and SS2 (gray) limits, dashed black line represents the LIA limit and the dash-dotted black line to the contact glacier-moraine in 1964.

The evolution of connectivity between 1964 and 2009 is quantified in figure 20 in terms of the relationship between the degree of pit filling and the upslope contributing area for different values of the Holmgren routing parameters (equation 2).

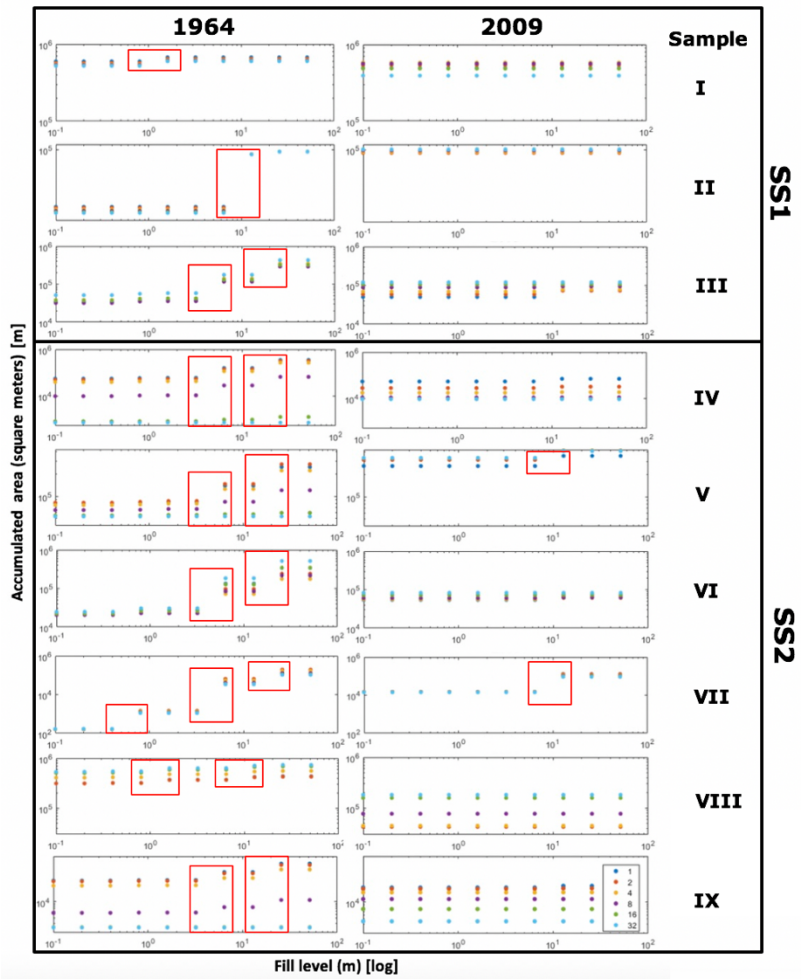

Figure 20: hydrological sediment connectivity quantification in 1964 and 2009 for selected regions highlighted in figure 18. Point colors refer to the Holmgren flow routing parameters and the red squares to the increases in upslope contributing area.

In 1964 the sediment connectivity in our study area is characterized by a general disconnectivity state both above and below the LIA limit. Figure 20 shows that all sampled locations, reflecting the potential barriers identified in figure 15, have one or more abrupt increases in basin contributing area showing their buffering effect on hydrological paths. Given this, is it also important to note that all transitions are higher than the DEM related noise suggested by the σ_{2009} (table 5), demonstrating the presence of natural rather than artificial disconnections.

The quantification of the buffers affecting the hydrological sediment connectivity of SS1 in 1964 (samples I-III on figure 20) did not show important sink strength. At the LIA limit region (I on figure 20) and on the morainic bastion (II in figure 20) the perfect connection is achieved through a single increase at, respectively, 1.6 m and 10.3 m of fill. In contrast, the hydrological connectivity on the alluvial fan (III in figure 20) is characterized by two increases at 1.7 m and 13 m, suggesting the presence of a more complex topography. In 2009, the hydrological sediment connectivity has strongly improved as the fill levels necessary to overcome obstacles are no longer present. The responsible mechanism is the gully headward erosion that, due to the progressive hydrological base level fall associated with the glacier thinning, generated a complete upstream basin reorganization on the morainic bastion. During the reconfiguration of the subsystem, it is also possible to observe the stronger sensibility to the Holmgren parameter probably suggesting the presence of a smoother aspect of slope at the end of the transition. This fact is more pronounced at the LIA limit and on the alluvial fan, whereas on the morainic bastion the flow is still channelized indicating the influence of the gully headward erosion.

On the other hand, the SS2 samples in 1964 (IV-IX on figure 20) are all characterized by two or more increases in upslope contributing area, between 2.2-5.5 m and 10.3-11.7 m of fill, except for the morainic bastion summit (VIII on figure 20) which have another little increase at 0.8 m. This fact highlights that, at the beginning of the study, numerous buffers affected the fluvial system making the SS2 more disconnected than SS1. Concerning the Holmgren parameter, in general we find a more concentrated flow on the morainic bastion compared to the lower LIA section. Similar to SS1, even the SS2 show an evolution shaped by the development of the drainage network. In 2009, the efficiency of the hydrological sediment connectivity strongly improved because most of the sampled locations show the disappearance of the barriers (IV, VI, VIII, IX on figure 20) or a strong reduction of their strength (V and VII on figure 20). In these latter cases, the continued existence of buffers is due to, respectively, the bedrock exposure and the crest of the morainic bastion. Nevertheless, at the light of the limited extention of the gully headward erosion showed on figure 17, we may conclude that this process played an important role especially on the lower LIA section, while on the morainic bastion it is rather the upslope basin reorganization which drove the improvement of the connectivity. The combination of these mechanisms allowed to change the spatial configuration of the geomorphic subsystem and the transition to a more diffuse flow. However, note that on the LIA limit region flow is anyway concentrated and it may be related to the recent headward erosion affecting the flatter accumulation at the gully head (I on figure 17F). In contrast, the marked diffused flow characterizing the alluvial fan (IX on figure 20) confirm its buffer effect related to the gentler gradient reducing the connectivity between the slope and the proglacial margin.

3.3 Terrestrial laser scanning surveys and present geomorphological changes

3.3.1 RiscanPro's multistation adjustment

Table 7 shows the RMS errors for the aligned scans using the multistation adjustment.

Table 7: MSA results in term of individual and mean RMS error.

	RMSE [m]	
	Scan day	
Scan Position	August 13th	August 20th
1	±0.007	±0.011
2	±0.002	±0.011
3	±0.011	±0.009
4	±0.004	±0.012
Mean	±0.006	±0.012

The RMS error is between ±0.002 m and ±0.012 m, an interval largely smaller than our initial ±5 cm threshold limit, and follows a normal distribution. This fact suggests the accuracy by which we identified the homologues point pairs on each point cloud during the co-registration.

3.3.2 Surface geomorphological changes

The M3C2 distance computation results show that some surficial geomorphological changes occurred between August 13th and 20th 2017, but the significant ones are mainly concentrated on the morainic bastion and on the gully systems (figure 21).

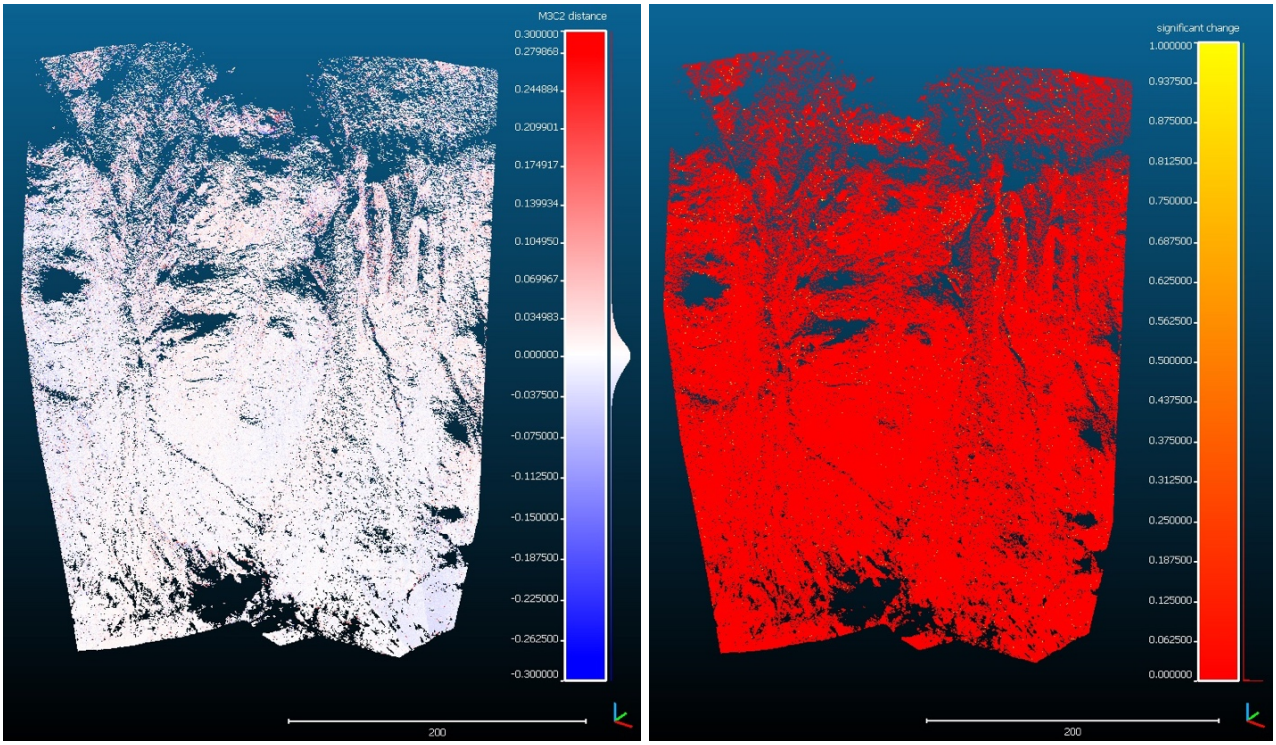

Figure 21: CloudCompare's M3C2 distance and significative surficial changes (95% LoD; yellow points) between August 13th and 20th 2017.

Surface changes were low in magnitude, with 98.6% of the surface elevation change between -0.2 and +0.2 m, of which 50% ranged between -0.01 and +0.01 m (figure 22).

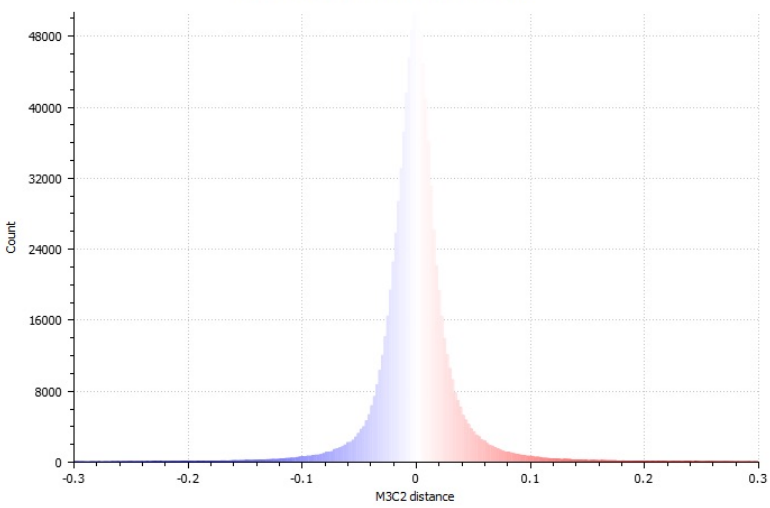

Figure 22: histogram of measured elevation changes using the M3C2.

Recorded daily precipitation (figure 23) are characterized by low magnitude rainfall episodes mainly during the nights. The maximum amount of precipitation occurred the 10th of August, just before our first lidar survey, with a cumulative precipitated water of 12 mm. During the next days, four weaker rainfall events followed with total amounts of precipitation between 2.2 and 5.8 mm. This could be the reason for the low geomorphological activity detected within the lidar surveys.

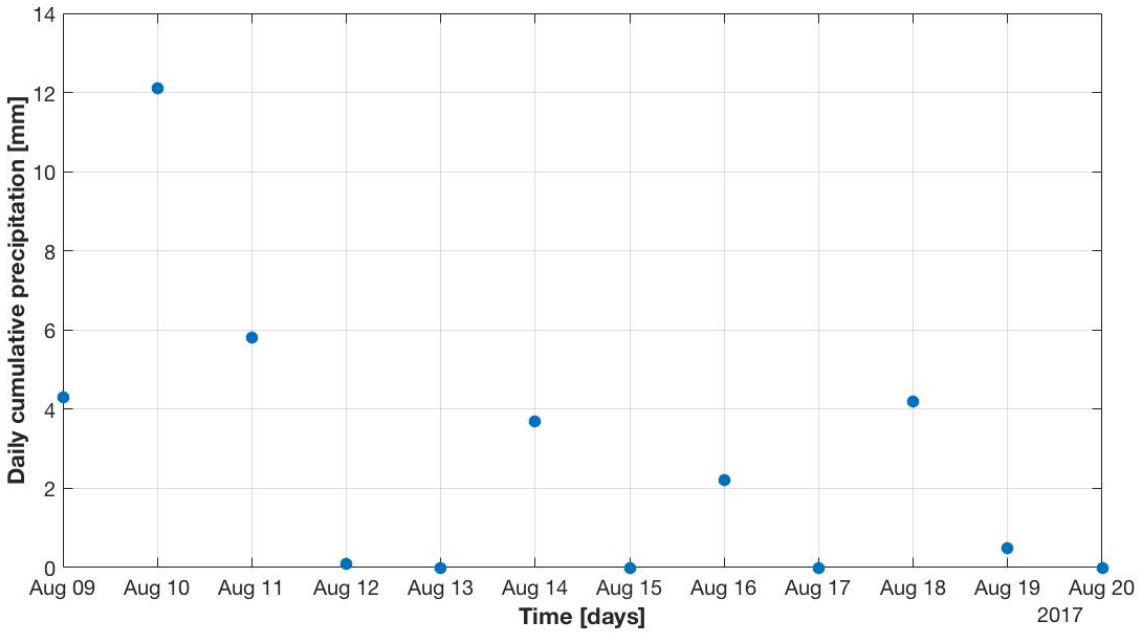

Figure 23: rainfall amounts at the Otemma's climatic station during the lidar survey campaign.

4. Discussion

4.1 Climatic evolution and the geomorphic response of the lateral moraine

During the 20th century, the MAAT at the GSB climatic station increased of about +1.7°C. This change was not distributed evenly, with a warmer period in the 1940s, a relative cooler phase intervened from the mid-1950s and the beginning of the 1980s, and finally again a more intense warmer period during the 1980s which, with weaker rates, continues until today (figure 12; OcCC, 2007; Haeberli and Beniston, 1998). This climatic evolution trend is the same experienced by the rest of the European Alps (Bauder et al., 2007; Fischer et al., 2015). The MAAT increase can have severe repercussions for the hydrological cycle in high mountain regions because it could rise the zero-isotherm degree towards higher elevations shifting the precipitation state and impacting glaciers mass balances (Beniston, 2003; Barnett et al., 2005; Scherrer and Appenzeller, 2006). In fact, since the end of the LIA, European glacier mass balances have closely followed MAAT trends (Houghton et al., 2001, Bauder et al., 2007). The result is that most Swiss glaciers have retreated continually through the period 1960 to present with exception of advances during the 1970s and early 1980s. The Glacier d'Otemma is one of a small number of glaciers that did not respond to this cooler and snowier period (figures 2, 12 and 13). This is because the glacier has a long distance between the ablation and the accumulation zones and a relatively low gradient valley bottom; the cooler period of the 1970s and 1980s was not long enough for any increase in accumulation to propagate to the snout before rapid warming and increased ablation become dominant in the 1980s (Hoelzle et al., 2003; Haeberli et al., 2007).

As the Glacier d'Otemma was in continuous retreat, it was possible to understand the way in which the moraine system has responded to continuous glacial debuttressing. It is recognized that glacier retreat exposes steep valley sidewalls covered with morainic deposits, or debris-mantled slopes, commonly over-steepened and so prone to erosion (Ballantyne, 2002a,b). Our historical geomorphological results (figures 16 and 17) showed how in parallel with glacier thinning, there was a tendency to gully erosion and where these gullies connected with the glacier surface and, eventually with further glacier thinning, the valley bottom, there was the formation of alluvial fans (figures 16 and 17). The landscape began to respond as soon as the glacier started to thin, that is as soon as base level fall began (Cossart and Fort, 2008; Porter et al., 2010), and continued until there is no more glacier to melt out highlighting the impact of climate warming on the ice body. Consequently, gully erosion was encouraged (figure 16, 17 and 19). There was also evidence of mean slope gradient decrease, and sediment down-wasting towards the alluvial fans forming at the gully toes (figures 15B and 15D) (Harvey, 1977; Curry et al., 2006). When all the glacier melted, our results suggests that the subsystems are still affected by gullying (figures 16D, 16E, 16F and 17D). This fact is related to the geomorphic evolution of the alluvial fans, which represent now the new hydrological base level for the subsystems.

Past research has focused on paraglacial geomorphology, and the development of landforms sequences in space from retreat of the glacier terminus, to explain qualitatively how recently deglaciated landscapes evolved once exposed to atmospheric conditions (e.g. Mercier, 1997; Curry, 2000). They found that evolution to a more stable configuration is effectively achieved by fluvial erosion and, in particular, by repeated debris flows (Gardner, 1982; Eyles and Kocsis, 1988). These latter are massive downslope movement of sediments mixed with water, triggered by rise in porewater pressures and consequent flow (Innes, 1983). This process involves three prerequisites (Ballantyne and Benn, 1994): (i) a steep topography of at least 30° or a changing hydrological base level; (ii) strong availability of unconsolidated debris, that usually are supplied by inter-gully walls; and finally (iii) removal of deposited sediment by water. In our subsystems, sediments are largely available because the Glacier de la Grande Lire morainic bastion and the morainic material covering the LIA section of the hillslope represent two important sources. In addition, permafrost thaw may increase

sediment availability due to loss of cohesion (Heaberli et al., 1997; Huggel et al., 2012). Water may be sourced from intense rainfalls, spring snowmelt and/or dead-ice melt (Theakstone, 1982; Haeberli and Naef, 1988; Haeberli et al., 1997). In our case, we found a strong relationship between fluvial processes and climatic agents because, in addition to glacial debuttressing, most of the gully induced geomorphological activity is likely triggered by metereological water.

As a result of fluvial processes, the final form of mature and geomorphological stable sediment-mantled slopes is characterized by three different sectors: an upper zone of exposed bedrock resulting from downslope sediment evacuation, a central zone where water flows in a concentrated way and, finally, several coalescent alluvial fans at hillslope feet built up by the perennial deposition of sediment reworked during debris flow events (Chorley and Kennedy, 1971; Schrott et al., 2003). The SS2 seems to correspond most clearly to this organization. For SS1, the thick sediment layer composing the morainic bastion prevents the bedrock exposure on the upper gully head section (figures 1 and 16F). The morainic bastion, which acts as main sediment source, makes this study different compared to the previous ones, not only because it shapes the geomorphic evolution but also because it influences the paraglacial period length. The length of time by which a glacial landscape responds after glacier recession has been described by Cruden and Hu (1993) using a theoretical exhaustion model. Starting from this mathematical simulation, Ballantyne (1995) and Curry (1999) demonstrated that debris-mantles slopes complete their paraglacial cycle rapidly in 50-200 years since deglaciation. However, in our case, is it logical to expect that the presence of the morainic bastion, increasing the unconsolidated sediment availability, might significantly extent the length of the paraglacial period.

4.2 Sediment cascade and hydrological connectivity response to glacial debuttressing

Similar to Cossart and Fort (2008), at the beginning of our study, the sediment cascades associated with the subsystems were affected by several intermediate sinks obstructing sediment flux to the valley bottom (figures 15 and 20) and diminishing their effective catchment areas (Harvey, 2002). These latter were composed of inherited glacial landforms, including a discontinous LIA ridge that partially breaks up the slope, as observed by others (e.g. Knight et al. 2007; Cossart and Fort, 2008; Lane et al., 2017), and by barriers constructed due to the interaction between paraglacial sediment reworking and the local topography. Sediment connectivity is dynamic because it changes in response to erosion and deposition, processes which itself regulates (Hugget, 2007; Fryirs, 2013). Geomorphological evolution is typically very dynamic during the paraglacial period, such that sediment connectivity may progress towards worst or better conditions. On the one hand, the combination of unconsolidated sediments and liquid water derived by rainstorms and snowmelt may produce large landslides whose deposition could temporary reduce sediment flux downstream (Maede, 1982; Fryirs et al., 2007). On the other hand, the filling of sediment sinks and erosion induced by gullying may significantly increase the ease of sediment transfer down the hillslope (Cossart and Fort, 2008). This latter case was observed in our study area between 1964 and 2009. Progressive disappearance of intermediate sinks allowed the increase of hydrological connectivity, with upslope contributing area increasing and the drainage network expanding upslope (figure 18, 19 and 20). This process, especially for SS1, was strictly driven by base level fall linked to the gradual glacier thinning (figures 16 and 17). Our results therefore confirm the conclusions of Lane et al. (2017) pointing out that gullying can be an important process in breaching features that disconnect downslope sediment flux, such morainic ridges. Connection still requires running water (Clague, 1986; Beylich et al., 2006) and in this case the Glacier de la Grande Lire may have provided water. Nevertheless, our TLS surveys (figure 21) showed that no significative changes occurred during the period within scans suggesting, as expected, the weak hydrological force exerted by the glacier meltwater and by the fallen precipitation (figure 23). This means, following Wolman and Miller (1960), that connectivity is not uniform over time but strongly related to magnitude-frequency relationship of a determined

processs. The works of Fryirs (2013) and Bracken et al. (2015) showed the importance of high magnitude events in activating the sediment cascade. In this case, the removal of disconnecting features has a double effect: not only does it allow flux more readily through a point in the landscape; it can also reorganize drainage basin areas upstream, potentially increasing (or decreasing) upslope contributing area and in turn increasing (or decreasing) erosion potential.

The results suggest that gullying, if it is not countered by sediment supply, can lead to exposure of undelying bedrock. As a direct consequence this may lead to topographic obstacles that then reduce connectivity and which are more resistance to erosion. This is exactly what happened in SS2 where, even if during the study period the overall sediment connectivity has improved, bedrock exposure slowed down gullying preventing perfect connection on its most upslope section (figures 17E and 20). In contrast, SS1 experienced the opposite because connection to the overlying morainic bastion, in addition to increase supply sediment rates to alluvial fan, prevented the exposure of bedrock obstacles and so disconnection (figures 16F and 20).

Alluvial fans are the final accumulation zones where mass movements deposit reworked sediments because it is rare that debris flows triggered on sidewalls directly reach the proglacial stream system (Becht, 1995; Curry, 2000). Once the glacier completely melted out, they control the hydrological base level of the gully systems developed on the hillslope (Harvey, 2001). Schrott et al. (2006) studied the alluvial fan buffering effect along a valley, and found a clear relationship between deglaciation time and their effectiveness in storing sediments. In the lower parts of deglaciated catchments, alluvial fans broke the hillslope-valley floor connection because stabilization also resulted in progressive revegetation. In contrast, in the upper parts of deglaciated catchments, even if they intercept down-wasting sediments reducing the overall connectivity, their sink effect is less pronounced due to the instable deposits left by the more recent deglaciation and not yet reworked. In fact, we showed that alluvial fans in the most recent studied dates are poorly characterized by vegetation colonization suggesting that geomorphological processes may still affect these landforms. However, even without vegetation, alluvial fans have reduced slopes, tend to be diffusive in hydrological terms and are commonly well-drained, all of which will lead to their effectiveness in decoupling valley side slopes from the stream bottom (figure 18; Fryirs and Brierley, 1999; Harvey, 2001). Erosion of alluvial fan toes is ultimately controlled by proglacial fluvial activity, allowing sediment transfert between the hillslope and the proglacial alluvial plain (Harvey, 1977, 1996; Lisenby and Fryirs, 2017). We were able to identify some erosion along the alluvial fan toe at the interface between the lateral moraine and the alluvial plain (figures 16D and 17F) linked to the development of the braided proglacial stream when the glacier completely disappeared. During this event, finer sediments will be most rapidly reworked, while gravels and boulders will move more slowly in a sequence of intermittent steps, each step associated with a peak in stream discharge (Caine, 1974). Such erosion could locally increase fan slope and potentially also encourage gully erosion upstream.

4.3 Weaknesses and perspectives

Permafrost thaw, resulting from progressive MAAT increase and decline of snow accumulation during winter in high mountain regions, is an important aspect to consider because it could increase the availability of unconsolidated sediments (Haeberli, 1973). There is no historical permafrost detection analysis (e.g. ERT,…) in our study area but, founding on studies in nearly valleys (e.g. Lambiel and Reynard, 2001; Lambiel et al., 2016) and on permafrost simulation models (Deluigi et al., 2017) that fix the actual lower limit of the discontinuous permafrost belt at the LIA altitude, on the constant MAAT increase since 1900 (figure 12), on the snow cover decline since 1980 (figure 13) and on the SSE exposition of the lateral moraine (figure 1), we could suppose that the lower permafrost limit progressively raised towards higher elevations. Its degradation may be potentially considered, in addition to the morainic bastion, another source of unconsolidated sediment suppling the lower LIA section in our study area.

For these reasons, additional data concerning sediment releases from the Otemma's water intake and permafrost monitoring would have provided more information on the evolution of catchment' sediment budget and the influence exerted by permafrost thaw on sediment delivery.

5. Conclusions

Observations of the historical geomorphological changes during the glacial debuttressing phase, in a context of rapid glacial recession, showed important considerations regarding both LIA lateral moraine paraglacial and sediment connectivity evolution. Our results suggest that these two notions are in a close relationship generating, following Hugget (2007), a process-form system. In fact, during the glacier debuttressing phase, landscape adjustment to non-glacial conditions changes the hillslope landforms assemblage impacting, at the same time, the strength of the intermediate sediment storages. In this context, we identified fluvial process, especially gullying activated in response to the progressive glacier thinning, as the main agent driving the relationship.

Due to gully development, the two subsystems evolved into a sediment cascade resembling that of a torrential system: an upper source zone, represented by the morainic bastion and the morainic layer covering the valley sidewall; a gullyed channel mainly activated during high magnitude rainfall events; and, finally, a lower accumulation zone consisting of alluvial fans and the proglacial alluvial plain. Alluvial fans form initially on the glacier surface until the glacier has thinned down to the level of the proglacial braid plain. The degree of connection to elements of the landscape upstream may be important as this influence sediment supply, important not only for maintaining sediment flux, but also preventing the development of bedrock disconnection and maintainin alluvial fan formation.

The two subsystems studied experienced different gully headward erosion intensities during the glacial debuttressing phase, resulting in two different states of hydrological connectivity. In one hand, SS1 experienced gully extension towards the morainic bastion destroying, at the same time, the intermediate sinks. In this case, the progressive hillslope denudation led to the improvement of the overall sediment connectivity and the absence of buffers at the interaction with the morainic bastion allowed balancing of the gully channel-floor erosion with maintained sediment supply. On the other hand, in SS2, although the gully development resulted in the loss of the initial intermediate storages improving the general connectivity of the subsystem, continued denudation exposed bedrock patches which slowed the development of the gully system which in turn created disconnection. In both cases, fluvially down-wasted sediments depositated at the hillslope base generated diffuse flow and disconnection.

We may conclude that during the paraglacial period gully headward erosion is a fundamental process that improve the overall sediment connectivity but, if the progressive hillslope denudation is not combined with sediment supply, exposure of local bedrock features may generate important disconnectivities. In addition, the work established that the hydrological connectivity approach developed by Lane et al. (2017) is a powerful tool for quantifying how connection evolves following glacier debuttressing.

6. Bibliography

Abermann, J., Fischer, A., Lambrecht, A. & Geist, T. (2010). On the potential of very high-resolution repeat DEMs in glacial and periglacial environments. *The Cryosphere*, 4, 53-65. DOI: 10.5194/tc-4-53-2010.

Aguilar, M.A., Aguilar, F.J., Fernandez, I. & Mills, J.P. (2013). Accuracy assessment of commercial self-calibrating bundle adjustment routines applied to archival aerial photogrammetry. *The Photogrammetric Record*, 28, 96-114. DOI: 10.1111/j.1477-9730.2012.00704.x.

Arnold, N. (2010). A new approach for dealing with depressions in digital elevation models when calculating flow accumulation values. *Progress in Physical Geography: Earth and Environment*, 34, 781-609. DOI: 10.1177/0309133310384542.

Ballantyne, C.K. & Benn, D.I. (1994). Paraglacial slope adjustment and resedimentation following glacier retreat, Fabergstolsdalen, Norway. *Arctic and Alpine Research*, 26, 255-169. DOI: 10.2307/1551938.

Ballantyne, C.K. (1995). Paraglacial debris cone formation on recently deglaciated terrain. *The Holocene*, 5, 25-33. DOI: 10.1177/095968369500500104.

Ballantyne, C.K. (2002a). Paraglacial geomorphology. *Quaternary Science Reviews*. 21, 1935-2017. DOI: 10.1016/S0277-3791(02)00005-7.

Ballantyne, C.K. (2002b). A general model of paraglacial landscape response. *The Holocene*, 12, 371-376. DOI: 10.1191/0950683602hl553fa.

Bakker, M. and Lane, S.N. (2017). Archival photogrammetric analysis of river-floodplain systems using Structure from Motion (SfM) method. *Earth Surface Processes and Landforms*, 42, 1274-1286. DOI: 10.1002/esp.4085.

Barnett, T.P., Adam, J.C. & Lettenmaier, D.P. (2005). Potential impacts of a warming climate on water availability in snow-dominated regions. *Nature*, 438, 303-309. DOI: 10.1038/nature04141.

Barnhart, T.B. & Crosby, B.T. (2013). Comparing two methods of surface change detection on an evolving thermokarst using high-temporal-frequency terrestrial laser scanning, Selewik river, Alsaka. *Remote sensing*, 5, 2813-2837. DOI: 10.3390/rs5062813.

Bauder, A., Funk, M. & Huss, M. (2007). Ice-volume changes of selected glaciers in the Swiss Alps since the end of the 19th century. *Annals of Glaciology*, 46, 145-149. DOI: 10.3189/172756407782871701

Baeriswyl, P.-A. and Rebetez, M. (1997). Regionalization of precipitation in Switzerland by means of principal component analysis. *Theoretical and Applied Climatology*, 58, 31-41. DOI: 10.1007/bf00867430.

Beawert, H. & Morche, D. (2014). Coarse sediment dynamics in a proglacial fluvial system (Fagge River, Tyrol). *Geomorphology*, 218, 88-97. DOI: 10.1016/j.geomorph.2013.10.021.

Becht, M. (1995). Slope erosion processes in the Alps. In: Slaymaker, O. (ed.), *Steepland Geomorphology* (pp. 45-61). Chichester: John Wiley and Sons.

Beylich, A.A., Etienne, S., Etzelmüller, B., Gordeev, V.V., Käyhkö, J., Rachold, V., Russell, A.J., Schmidt, K.-H., Saemundsson, P., Tweed, F.S. & Warburton, J. (2006). The European Science Foundation (ESF) network SEDIFLUX – an introduction and overview. *Geomorphology*, 80, 3-7. DOI: 10.1016/j.geomorph.2005.11.013.

Beniston, M. (2003). Climatic change in mountain regions: A review of possible impacts. *Climatic Change*, 59, 5-31. DOI: 10.1023/A:1024458411589.

Borselli, L., Cassi, P. & Torri, D. (2008). Prologomena to sediment and flow connectivity in the landscape: A GIS and field numerical assessment. *Catena*, 75, 268-277. DOI: 10.1016/j.catena.2008.07.006.

Bracken, L.J., Turnbull, L., Wainwright, J. & Bogaart, P. (2015). Sediment connectivity: a framework for understanding sediment transfer at multiple scales. *Earth Surface Processes and Landforms*, 40, 177-188. DOI: 10.1002/esp.3635.

Brardinoni, F. & Hassan, M.A. (2006). Glacial erosion, evolution of river long profiles, and the organization of processes domains in mountain drainage basins of coastal British Columbia. *Journal of Geophysical Research*, 111, F01013, 1-12. DOI: 10.1029/2005JF000358.

Brasington, J., Rumsby, B.T. & Mcvey, R.A. (2003). Monitoring and modeling morphological change in a braided gravel-bed river using high resolution GPS-based survey. *Earth Surface Processes and Landforms*, 25, 973-990. DOI: 10.1002/1096-9837(200008)25:9<973::AIDESP111>3.0.CO;2-Y.

Brodu, N. & Lague, D. (2012). 3D terrestrial lidar data classification of complex natural scenes using a multi-scale dimensionality criterion: Applications in geomorphology. *Journal of Photogrammetry and Remote Sensing*, 68, 121-134. DOI: 10.1016/j.isprsjprs.2012.01.006.

Burri, M., Allimann, M., Chessex, R., Dal Piaz, G.V., Delle Valle, G., Du Bois, L., Gouffon, Y., Guermani, A., Hagen, D., Krummenacher, D. & Looser, M.-O. (1999). Feuille 1346/1366 Chanrion-Mt-Vélan, carte 101 (Geological Atlas of Switzerland 1:25'000). Wabern: SwissTopo.

Caine, N. (1974). The geomorphic processes of alpine environment. In Ives, J.D. & Barry, R.C. (eds.), *Arctic and Alpine environments* (pp. 721-749). London: Methuen.

Carrivick, J.L., Geilhausen, M., Warburton, J., Dickson, N.E., Carver, S.J., Evans, A.J. & Brown, L.E. (2013). Contemporary geomorphological activity throughout the proglacial area of an alpine catchment. *Geomorphology*, 188, 83-95. DOI: 10.1016/j.geomorph.2012.03.029.

Castillo, C., Taguas, E.V., Zarco-Tejada, P., James, M.R. and Gomez, J.A. (2014). The normalized topographic method: an automated procedure for gully mapping using GIS. *Earth Surface Processes and Landforms*, 39, 2002-2015. DOI: 10.1002/esp.3595.

Cavalli, M., Trevisani, S., Comiti, F. & Marchi, L. (2013). Geomorphometric assessment of spatial sediment connectivity in small Alpine catchments. *Geomorphology*, 188, 31-41. DOI: 10.1016/j.geomorph.2012.05.007.

Chorley, R.J. & Kennedy, B.A. (1971). *Physical geography: A system approach*. London: Prentice-Hall International Inc.

Church, M. & Ryder, J.M. (1972). Paraglacial sedimentation: a consideration of fluvial processes conditioned by glaciation. *Geological Society of America Bulletin*, 83, 3059-3072. DOI:10.1130/0016-7606(1972)83[3059:psacof]2.0.co;2.

Clague, J.J. (1986). The Quaternary stratigraphic record of British Columbia – evidence for episodic sedimentation and erosion controlled by glaciation. *Canadian Journal of Earth Sciences*, 23, 885-894. DOI: 10.1139/e86-090.

CloudCompare (2015). *Noise filter*. www.cloudcompare.org/doc/wiki/index.php?title =Noise_filter.

Cossart, E. et Fort, M. (2008). Sediment release and storage in early deglaciated areas: Towards an application of the exhaustion model from the case of Massif des Ecrins (French Alps) since the Little Ice Age. *Norwegian Journal of Geography*, 62, 115-131. DOI: 10.1080/00291950802095145.

Cruden, D.M. & Hu, X.Q. (1993). Exhaustion and steady-state models for predicting landslide hazards in the Canadian Rocky Mountains. *Geomorphology*, 8, 279-285. DOI: 10.1016/0169-555x(93)90024-x.

Curry, A.M. (1999). Paraglacial modification of slope form. *Earth Surface Processes and Landforms*, 24, 1213-1228. DOI: 10.1002/(sici)1096-9837(199912)24:13<1213::aid-esp32>3.3.co;2-2.

Curry, A.M. (2000). Observation on the distribution of paraglacial reworking of glacigenic drift in western Norway. *Norsk Geografisk Tidsskrift – Norwegian Journal of Geography*, 54, 139-147. DOI: 10.1080/002919500448512.

Curry, A.M., Cleasby, V. & Zukowskyj, P. (2006). Paraglacial response of steep, sediment-mantled slopes to post-'Little Ice Age' glacier recession in the central Swiss Alps. *Journal of Quaternary Science*, 21, 211-225. DOI: 10.1002/jps.954.

Deluigi, N., Lambiel, C. & Kanevski, M. (2017). Data-driven mapping of the potential mountain permafrost distribution. *Science of the Total Environment*, 590-591, 370-380. DOI: 10.1016/j.scitotenv.2017.02.041.

Eyles, N., & Kocsis, S. (1988). Sedimentology and clast fabric of subaerial debris flows facies in a glacially influenced alluvial fan. *Sedimentary Geology*, 65, 196-197. DOI: 10.1016/00370738(88)90098-x.

Fischer, M., Huss, M., Bardoux, C., & Hoelzle, M. (2014). The new Swiss Glacier inventory SGI2010: Relevance of using high-resolution source data on areas dominated by very small glaciers. *Arctic, Antarctic, and Alpine Research*, 46, 933-945. DOI: 10.1657/1938-4246-46.4.933.

Fischer, M., Huss, M. & Hoelzle, M. (2015). Surface elevation and mass changes of all Swiss glaciers 1980-2010. *The Cryosphere*, 9, 525-540. DOI: 10.5194/tc-9-525-2015.

Fryirs, K. & Brierley, G.J. (1999). Slope-channel decoupling in Wolumla catchment, New South Wales, Australia: the changing nature of sediment sources following European settlement. *Catena*, 35, 41-63. DOI: 10.1016/S0341-8162(98)00119-2.

Fryirs, K., Brierley, G.J., Preston, N.J. & Kasai, M. (2007). Buffers, barriers and blankets: the (dis)connectivity of catchement scale cascade. *Catena*, 70, 49-67. DOI: 10.1016/j.catena.2006.07.007.

Fryirs, K. (2013). (Dis)Connectivity in catchment sediment cascades: a fresh look at the sediment delivery problem. *Earth Surface Processes and Landforms*, 38, 30-46. DOI: 10.1002/esp.3242.

Fonstad, M.A., Dietrich, J.T., Courville, B.C., Jensen, J.L. and Carbonneau, P. (2013). Topographic structure from motion: a new development in photogrammetric measurement. *Earth Surface Processes and Landforms*, 38, 421-430. DOI: 10.1002/esp.3366.

Gabbud, C., Micheletti, N. & Lane, S.N. (2015). Lidar measurement of surface melt for a temperate Alpine glacier at hourly scales. *Journal of Glaciology*, 61, 963-974. DOI: 10.3189/2015JoG14J226.

Gabbud, C., Micheletti, N. and Lane, S.N. (2016). Response of a temperate Alpine valley glacier to climate change at a decadal scale. *Geografiska Annaler*, 98, 81-95. DOI: 10.1111/geoa.12124.

Gardner, J.S. (1982). Alpine mass wasting in contemporary time: some exemples from the Canadian Rocky Mountains. In Thorn, C.E. (ed.), *Space and Time in Geomorphology* (pp.171-192). Allen and Unwin: London.

Girardeau-Montaut, D., Roux, M., Marc, R., & Thibault, G. (2005). Change detection on points cloud data acquired with a groud laser scanner. *International Archives of Photogrammetry, Remote Sensing and Spatial Information Sciences*, 36, 30-35.

Glaciers Monitoring in Switzerland (GLAMOS) (2016). Glacier d'Otemma, Bagnes (VS). *Swiss glacier monitoring network*. www.swiss-glaciers.glaciology.ethz.ch/glaciers/otemma.

Gomez, C., Hayakawa, Y. and Obanawa, H. (2015). A study of Japanese landscapes using structure from motion derived DSMs and DEMs based on historical aerial photographs: new opportunities from vegetation monitoring and diachronic geomorphology. *Geomorphology*, 242, 11-20. DOI: 10.1016/j.geomorph.2015.02.021.

Goodwin, N., Armston, J.D., Muir, J. & Stiller, I. (2017). Monitoring gully change: A comparison of airborne and terrestrial laser scanning using a case study from Aratula, Queensland. *Geomorphology*, 282, 195-208. DOI: 10.1016/j.geomorph.2017.01.001.

Haeberli, W. (1973). Die Basis-Temperatur der winterlichen Schneedecke als möglicher Indikator für die Verbreitung von Permafrost. *Zeitschrift für Gletscherkunde und Glazialgeologie*, 9, 221-227.

Haeberli, W. & Naef. F. (1988). Murgänge im hochgebirge. *Die Alpen*, 64, 331-343.

Haeberli, W., Wegmann, M. & Vonder Mühll, D. (1997). Slope stability problems related to glacier shrinkage and permafrost degradation in the Alps. *Ecologae Geologicae Helvetiae*, 90, 407-414. DOI: 10.5169/seals-168172.

Haeberli, W. et Beniston, M. (1998). Climate change and its impacts on glaciers and permafrost in the Alps. *Ambio*, 27, 258-265.

Haeberli, W., Hoelzle, M., Paul, F. & Zemp, M. (2007). Integrated monitoring of mountains glaciers as key indicators of global climate change: the European Alps. *Annals of Glaciology*, 46, 150-160. DOI:

Hancock, G.R. (2006). The impact of different gridding methods on catchment geomorphology and soil erosion over long timescales using a landscape evolution model. *Earth Surface Processes and Landforms*, 31, 1035-1050. DOI: 10.1002/esp.1306.

Harvey, A.M. (1977). Coupling between hillslope gully systems and stream channels in the Howgill Fells, northwest England: temporal implications. *Géomorphologie: relief, processus, environnement*, 3, 3-19. DOI: 10.3406/morfo.1997.897.

Harvey, A.M. (1996). Holocene hillslope gully systems in the Howgill Fells, Cumbria. In Anderson, M.G. & Brooks, S.M. (eds.), *Advances in Hillslope Processes – Volume 2* (pp. 731-752). Chichester: Wiley.

Harvey, A.M. (2001). Coupling between hillslopes and channels in upland fluvial systems: implications for landscape sensitivity illustrated from the Howgill Fells, northwest England. *Catena*, 42, 225-250. DOI: 10.1016/S0341-8162(00)00139-9.

Harvey, A.M. (2002). Effective timescale of coupling within fluvial systems. *Geomorphology*, 44, 175-201. DOI: 10.1016/S0169-555X(01)00174-X.

Heckmann, T., McColl, S. & Morche, D. (2016). Retreating ice: research in proglacial areas matters. *Earth Surface Processes and Landforms*, 41, 271-276. DOI: 10.1002/esp.3858.

Heritage, G.L., Milan, D.J., Large, A.R.G. and Fuller, I.C. (2009). Influence of survey strategy and interpolation model on DEM quality. *Geomorphology*, 112, 334-344. DOI: 10.1016/j.geomorph.2009.06.024.

Hoelzle, M., Haeberli, W., Dischl, M. & Peschje, W. (2003). Secular glacier mass balances derived from cumulative glacier length changes. *Global Planetary Change*, 36, 295-306. DOI: 10.1016/S0921-8181(02)00223-0.

Holmes, K.W., Chadwick, O.A. & Kyriakidis, P.C. (2000). Error in a USGS 20-meter digital elevation model and its impacts on terrain modelling. *Journal of Hydrology*, 233, 154-173. DOI: 10.1016/S0022-1694(00)00229-8.

Holmgren, P. (1994). Multiple flow direction algorithms for runoff modelling in grid based elevation models: an empirical evaluation. *Hydrological Processes*, 8, 327-334. DOI: 10.1002/hyp.3360080405.

Houghton, J.T., Ding, Y., Griggs, D.J., Noguer, M., van der Linden, P.J., Dai, X., Maskell, K. & Johnson, C.A. (2001). *Climate change 2001: the scientific basis. Contribution of Working Group I to the Third Assessment Report of the Intergovernmental Panel on Climate Change*. Cambridge: Cambridge University Press.

Huggel, C., Clague, J.J. & Korup, O. (2012). Is climate change responsible for changing landslide activity in high mountains?. *Earth Surface Processes and Landforms*, 37, 77-91. DOI: 10.1002/esp.2223.

Hugget, R.J. (2007). *Foundamentals of Geomorphology*. Routledge: London.

Innes, J.L. (1983). Debris flows. *Progress in Physical Geography*, 7, 469-501. DOI: 10.1177/030913338300700401.

James, M.R. & Robson, S. (2012). Straightforward reconstruction of 3D surfaces and topography with a camera: accuracy and geoscience application. *Journal of Geophysical Research. Earth Surface*, 117. DOI: 10.1029/2011JF002289.

James, M.R. & Robson, S. (2014). Mitigating systematic error in topographic models derived from UAV and ground-based image networks. *Earth Surface Processes and Landforms*, 39, 1412-1420. DOI: 10.1002/esp.3609.

Javernick, L., Brasington, J. and Caruso, B. (2014). Modeling the topography of shallow brided rivers using Structure-from-Motion photogrammetry. *Geomorphology*, 213, 166-182. DOI: 10.1016/j.geomorph.2014.01.006.

Jones, L.D. (2006). Monitoring landslides in hazardous terrain using terrestrial LIDAR: An example from Montserrat. *Quarterly Journal of Engineering and Hydrogeology*, 39, 371-373. DOI: 10.1144/1470-9236/06-009.

Kääb, A. & Vollmer, M. (2000). Surface Geometry, Thickness Changes and Flow Fields on Creeping Mountain Permafrost: Automatic Extraction by Digital Image Analysis. *Permafrost and Periglacial Processes*, 11, 315-326. DOI: 10.1002/1099-1530(200012)11:4<315::AID-PPP365>3.0.CO;2-J.

Kazhdan, M., Bolitho, M. & Hoppe, H. (2006). Poisson Surface Reconstruction. In K. Pothier & A. Sheffer (Eds.), *Eurographics Symposium on Geometry Processing* (pp. 61-70). The Eurographics Association. DOI: 10.2312/SGP/SGP06/061-070.

Knight, P.G., Jennings, C.E., Waller, R.I. & Robinson, Z.P. (2007). Changes in ice-margin processes and sediment routing during ice-sheet advance across a marginal moraine. *Geografiska Annaler*, 89, 203-215. DOI: 10.1111/j.1468-0459.2007.00319.x.

Küng, O., Strecha, C., Beyeler, A., Zuffrey, J.C., Floreano, D., Fua, P. and Gervaix, F. (2011). The Accurancy of Automatic Photogrammetric Techniques on Ultra-Light UAV Imagery. *International archives of the Photogrammetry, Remote Sensing and Spatial Information Sciences*, 38, 125-130. DOI: 10.5194/isprasrchives-XXXVIII-1-C22-125-2011.

Lague, D., Brodu, N. and Leroux, J. (2013). Accurate 3D comparison of complex topography with terrestrial laser scanner: Application to the Rangitikei canyon (N-Z). *ISPRS Journal of Photogrammetry and Remote Sensing*, 82, 10-26. DOI: 10.1016/j.isprsjprs.2013.04.009.

Lambiel, C. & Reynard, E. (2001). Regional modelling of present, past and future potential distribution of discontinous permafrost based on a rock glacier invoentory in the Bagnes-Hérémence area (Western Swiss Alps). *Norsk Geografisk Tidsskrift – Norwegian Journal of Geography*, 55, 219-224. DOI: 10.1080/00291950152746559.

Lambiel, C., Maillard, B., Kummert, B. & Reynard, E. (2016). Geomorphology of the Hérens valley (Swiss Alps). *Journal of Maps*, 12, 160-172. DOI: 10.1080/17445647.2014.999135.

Lambiel, C. & Tolon, P. (in press). Les glaciers du Haut Val de Bagnes au Petit Age Glaciaire. *Annales valaisannes, Actes du colloque Giétro 1818*, Martigny.

Lane, S.N., Richards, K.S. and Chandler, J.H. (1993). Developments in photogrammetry: the geomorphological potential. *Progress in Physical Geography*, 13, 306-328. DOI: 10.1177/030913339301700302.

Lane, S.N., Chandler, J.H. and Richards, K.S. (1994). Developments in monitoring and modeling small-scale river bed topography. *Earth Surface Processes and Landforms*, 19, 349-368. DOI: 10.1002/esp.3290190406.

Lane, S.N., Richards, K.S. & Chandler, J.H. (1996). Discharge and sediment supply controls on erosion and deposition in a dynamic alluvial channel. *Geomorphology*, 15, 1-15. DOI: 10.1016/0169-555X(95)00113-J.

Lane, S.N. (1998). The use of digital terrain modeling in the understanding of dynamic river systems. In: Lane, S.N., Richards, K.S. and Chandler, J.H. (eds), *Landform Monitoring, Modelling, and Analysis* (pp. 311-342). Chichester: John Wiley and Son.

Lane, S.N., James, T.D. and Crowell, M.D. (2000). Application of digital photogrammetry to complex topography for geomorphological research. *The Photogrammetric Record*, 16, 793-821. DOI: 10.1111/0031-868X.00152.

Lane, S.N., Westaway, R.M. & Hicks, D.M. (2003). Estimation of erosion and deposition volumes in a large, gravel-bed, braided river using synoptic remote sensing. *Earth Surface Processes and Landforms*, 28, 181-198. DOI: 10.1002/esp.483.

Lane, S.N., Reid, S.C, Westaway, R.M. and Hicks, D.M. (2004). Remotely sensed topographic data for river research: the identification, explanation and management of error. In: Kelly, R.E.J., Drake, N.A. and Barr, S.L. (eds), *Spatial Modelling of the Terrestrial Environment* (pp. 113-136). Chicester: John Wiley & Sons.

Lane, S.N., Widdison, P.E., Thomas, R.E., Ashworth, P.J., Best, J.L., Lunt, I.A., Sambrook Smith, G.H. & Simpson, C.J. (2010). Quantification of braided river channel change using archival digital image analysis. *Earth Surface Processes and Landforms*, 35, 971-985. DOI: 10.1002/esp.2015.

Lane, S.N., Bakker, M., Gabbud, C., Micheletti, N. & Saugy, J. N. (2017). Sediment export, transient landscape response and catchment-scale connectivity following rapid climate warming and Alpine glacier recession. *Geomorphology*, 227, 210-227. DOI: 10.1016/j.geomorph.2016.02.015.

Lane, S.N., Gabbud, C. & Micheletti, N. (2018). Reconstructing sediment connection in Alpine landscapes undergoing rapid glacier recession. EU COST Meeting, Connecteur, 26-28 March, Venice.

Lisenby, P.E. & Fryirs, K.A. (2017). Sedimentologically significant tributaries: catchment-scale controls on sediment (dis)connectivity in the Lockyer Valley, SEQ, Australia. *Earth Surface Processes and Landforms*, 42, 1493-1504. DOI: 10.1002/esp.4130.

Lowe, D.G. (1999). Object recognition from local scale-invariant features. In: *The Proceedings of the Seventh IEEE International Conference on Computer Vision*, 1150-1157.

Maede, R.H. (1982). Sources, sinks and storage of the river sediment in the Atlantic drainage of the United States. *Journal of Geology*, 90, 235-252. DOI: 10.1086/628677.

McColl, S. (2012). Paraglacial rock-slope stability. *Geomorphology*, 153, 1-16. DOI: 10.1016/j.geomorph.2012.02..15.

McColl, S. T. & Davis, T.R.H (2013). Large ice-contact slope movements: glacial buttressing, deformation and erosion. *Earth Surface Processes and Landforms*, 38, 1102-1115. DOI: 10.1002/esp.3346.

Mercier, D. (1997). L'impact du ruissellement sur les moraines latérales du Glacier du Roi (Collentthonga, Spitzberg, 79°N). *Norois*, 44, 549-566. DOI: 10.3406/noroi.1997.6817.

Mercier, D. (2008). Paraglacial and paraperiglacial landsystems: concepts, temporal scales and spatial distribution. *Géomorphologie: rélief, processus, environnement*, 14(4), 223-233. DOI: 10.4000/geomorphologie.7396.

Micheletti, N., Lambiel, C. & Lane, S.N. (2015a). Investigating decadal-scale geomorphic dynamics in an alpine mountain setting. *Journal of Geophysical Research: Earth Surface*, 120, 2155-2175. DOI: 10.1002/2015FH003656.

Micheletti, N., Lane, S.N. and Chandler, J.H. (2015b). Application of archival aerial photogrammetry to quantify climate forcing of Alpine landscapes. *The Photogrammetric Records*, 30, 143-165. DOI: 10.1111/phor.12099.

Micheletti, N., Chandler, J.H. and Lane, S.N. (2015c). Structure from Motion (SfM) photogrammetry. In Cook, S.J., Clarke, L.E. and Nield, J.M. (eds), *Geomorphological techniques*. London: British Society for Geomorphology.

Miller, P., Mills, J., Edwards, S., Bryan, P., Marsh, S., Mitchell, H. & Hopps, P. (2008). A robust surface matching technique for coastal geohazard assessment and management. *ISPRS Journal of Photogrammetry and Remote Sensing*, 65, 529-542. DOI: 10.1016/j.isprsjprs.2008.02.003.

Mölg, N. and Bolch, T. (2017). Structure-from-Motion using historical aerial images to analyse changes in glacier surface elevation. *Remote sensing*, 9, 1021-1038. DOI:10.3390/rs.9101021.

Moore, I.D., Grayson, R.B. & Ladson, A.R. (1991). Digital terrain modeling: a review of hydrological, geomorphological and biological applications. *Hydrological Processes*, 5, 3-90. DOI: 10.1002/hyp.3360050103.

OcCC (Organ consultatifs sur les Changements Climatiques) (2007). *Climate Change and Switzerland 2050. Expected Impacts on Environment, Society and Economy*. Bern.

Olsen, M.J., Kuester, F., Chang, B.J. & Hutchinson, T.C. (2010). Terrestrial laser scanning-based structural damage assessment. *Journal of Computing in Civil Engineering*, 23, 264-272. DOI: 10.1061/(ACE)CP.1943-5487.0000028.

Orwin, J.F. & Smart, C.C. (2004). Short-term spatial and temporal patterns of suspended sediment transfer in proglacial channels, Small River Glacier, Canada. *Hydrological Processes*, 18, 1521-1542. DOI: 10.1002/hyp.1402.

Paul, F., Kääb, A., Maisch, M., Kellenberger, T. & Haeberli, W. (2004). Rapid disintegration of Alpine glaciers observed within satellite data. *Geophysical Research Letters*, 31. DOI: 10.1029/1004GL020816.

Porter, P.R., Vatne, G., Ng, F. & Irvine-Flynn, T.D.L. (2010). Ice-marginal sediment delivery to the surface of a high-Arctic glacier: Austere Broggerbreen, Svalbard. *Geografiska Annaler*, 92, 437-449. DOI: 10.1111/j.1468-0459.2010.00406.x.

Quinn, P., Beven, K., Chevallier, P. & Planchon, O. (1991). The prediction of hillslope flow paths for distributed hydrological modelling using digital terrain models. *Hydrological Processes*, 5, 59-79. DOI: 10.1002/hyp.3360050106.

Rieger, W. (1998). A phenomenon-based approach to upslope contributing area and depressions in DEMs. *Hydrological Processes*, 12, 857-872. DOI: 10.1002/(sici)1099-1085(199805)12:6<857::aid-hyp659>3.0.co;2-b.

RIEGL Laser Measurements Systems (2015). *RIEGL VZ-6000 – 3D Ultra long range terrestrial laser scanner with online waveform processing*. RIEGL Laser Measurement Systems, Horn.

Scherrer, S.C. & Appenzeller, C. (2006). Swiss Alpine snow pack variability: major patterns and links to local climate and large-scale flow. *Climate Research*, 32, 187-199. DOI: 10.3354/cr032187.

Schiefer, E. & Gilbert, R. (2007). Reconstructing morphometric change in a proglacial landscape using historical aerial photography and automated DEM generation. *Geomorphology*, 88, 167-178. DOI: 10.1016/j.geomorph.2006.11.003.

Schrott, L., Hufschmidt, G., Hankammer, M., Hoffman, T. & Dikau, R. (2003). Spatial distribution of sediment storage types and quantification of valley fill deposits in an alpine basin, Reintal, Bavarian Alps, Germany. *Geomorphology*, 55, 45-63. DOI: 10.1016/s0169555x(03)00131-4.

Schrott, L., Götz, J., Geilhausen, M. & Morche, D. (2006). Spatial and temporal variability of sediment transfer and storage in an Alpine basin (Reintal valley, Bavarian Alps, Germany). *Geographica Helvetica*, 61, 191-200. DOI: 10.5194/gh-61.191.2006.

Schürch, P., Densmore, A.L., Rosser, N., Lim, M. & McArdell, B.W. (2011). Detection of surface change in complex topography using terrestrial laser scanning: Application to the Illgraben debris-flow channel. *Earth Surface Processes and Landforms*, 36, 1847-1859. DOI: 10.1002/esp.2206.

Schwanghart, W. & Kuhn, N.J. (2010). TopoToolbox: a set of Matlab functions for topographic analysis. *Environmental Modelling & Software*, 25, 770-781. DOI:10.1017/j.envsoft.2009.12.002.

Smith, M.W., Carrivick, J.L. & Quincey, D.J. (2016). Structure from motion photogrammetry in physical geography. *Progress in Physical Geography*, 40, 1-29. DOI: 10.1177/0309133315615805.

Theakstone, W.H. (1982). Sediment fans and sediment flows generated by snowmelt: observations at Austerdalsisen, Norway. *Journal of Geology*, 90, 583-588. DOI: 10.1086/628715.

Trevisani, S., Cavalli, M. & Marchi, L. (2012). Surface texture analysis of a high-resolution DTM: Interpreting an alpine basin. *Geomorphology*, 161, 26-39. DOI: 10.1016/j.geomorph.2012.03.031.

Uhlmann, M., Korup, O., Huggel, C., Fischer, L. & Kargel, J.S. (2013). Supra-glacial deposition and sediment flux of catastrophic rock-slope failure debris, south-central Alaska. *Earth Surface Processes and Landforms*, 38, 675-682. DOI: 10.1002/esp.3311.

Wackrow, R. and Chandler, J.H. (2008). A convergent image configuration for DEM extraction that minimizes the systematic effects by an inaccurate lens model. *The Photogrammetric Record*, 23, 6-18. DOI: 10.1111/j.1477-9730.2008.00467.x.

Westoby, M.J., Brasington, J. Glasser, N.F. Hambrex, M.J. and Reynolds, J.M. (2012). "Structure-from-Motion" photogrammetry: A low-cost, effective tool for geoscience applications. *Geomorphology*, 179, 300-314. DOI: 10.1016/j.geomorph.2012.08.021.

Wheaton, J.M., Brasington, J., Darby, S.E. and Sear, D.A. (2010). Accounting for uncertainty in DEMs from repeat topographic survey: improved sediment budgets. *Earth Surface Processes and Landforms*, 35, 136-156. DOI: 10-1002/esp.1886.

Wolman, M.G. & Miller, J.P. (1960). Magnitude and frequency of forces in geomorphic processes. *Journal of Geology*, 68, 54-74. DOI: 10.1086/626637.

Zemp, M., Haeberli, W., Hoelzle, M. & Paul, F. (2006). Alpine glaciers to disappear within decades?. *Geophysical Research Letters*, 33. DOI: 10.1029/2006GL026319.